Constraining Fault Friction and Stability with Fluid-Injection Field Experiments

Stacy Larochelle[1], Nadia Lapusta[1,2], Jean-Paul Ampuero[3], and Frédéric Cappa[3,4]

[1] Division of Geological and Planetary Sciences, California Institute of Technology, Pasadena, California 91125, USA.
[2] Division of Engineering and Applied Science, California Institute of Technology, Pasadena, California 91125, USA
[3] Université Côte d'Azur, IRD, CNRS, Observatoire de la Côte d'Azur, Géoazur, 06560 Sophia Antipolis, France
[4] Institut Universitaire de France, Paris, France

Contents of this file

Text S1 to S2
Table S1
Figures S1 to S29

Introduction

The following supporting information describes long-term simulations justifying our choice of initial conditions as well as further discussion on the lengthscale h_{ac} derived in the main text. We also provide additional figures that illustrate the evolution of all variables in the simulation and how certain combinations of parameters control the simulation results.

Text S1. Long-term simulations without tectonic or fluid pressure loading

In the models presented in this study, we prescribe initial conditions that are consistent with a dormant fault by starting with a highly healed fault (i.e., high initial value of the state variable θ_{ini}). This choice of initial conditions is justified by the long-term simulations without tectonic or fluid pressure loading shown in Figures S4-S7. The initial values affect some initial behavior/slip of the fault but, long-term, the fault heals under the near-constant values of shear stress, with a power-law decrease in slip rate as well as an increase in state variable over time; at long times, the value of the state variable is approximately equal to the healing time of the fault. This behavior can be predicted analytically: When the fault is well below steady-state ($V\theta/D_{RS} \ll 1$), $\dot{\theta} \sim 1$ and thus $\theta \sim t$. Moreover, with shear stress being almost constant, the rate-and-state friction coefficient is fixed and $\dot{f} = a\dot{V}/V + b/t = 0$, implying that $V \propto t^{-b/a}$. The initial conditions in the intermediate- and high-friction cases in this study are consistent with this behavior. In the low-friction case, although we do prescribe a high initial state variable and a low initial slip rate, the fault needs to be initially above steady state to match the measured slip behavior at the injection size and therefore not consistent with the behavior described above.

Text S2. h_{ac}: Estimate of slipping zone length at slip acceleration

In the main text, we derived an estimate of the slipping zone length at the time of slip acceleration (beginning of Stage 3). If $(\sigma - p)$ remained constant throughout the simulation, Eq. (11) would reduce to $h_{ac} \propto \mu D_{RS}/b$ which is similar to the condition for acceleration $k < k_b$ (where k is stiffness) in the spring-block slider model (Dieterich, 1992; Helmstetter & Shaw, 2009) and to the condition $h > L_b$ for acceleration on continuum fault segments that are far above steady-state (Rubin & Ampuero, 2005). Eq. (11) is also similar to the findings for seismic slip nucleation in slip-weakening friction models (Uenishi & Rice, 2003; Viesca & Rice, 2012) except that h_{ac} depends on pressure; specifically on the maximum value of pressure (at the injection site). The fact that this lengthscale does not depend - at least to first order - on the extent or shape of

the pore pressure distribution is also consistent with prior findings (Uenishi & Rice, 2003; Viesca & Rice, 2012). At the same time, h_{ac} is different from some of the discussed critical lengthscales, since it does not signify the transition to dynamic, inertially-controlled earthquake slip, but rather corresponds to the beginning of the different quasi-static slip stage in this particular experiment. The existence of h_{ac} is linked to the two-stage quasi-static slip process in the field experiment which the simulations are trying to emulate. The associated evolution of the friction coefficient - with sharp increase to a peak value, then near-linear decrease vs. slip with the slope of b, and then near-constant value - is likely related to the relatively rapid increase of the pore pressure at the injection site compared to the timescale of state variable evolution considered in this work.

To demonstrate that Eq. (11) holds, in Figures S12 and S14(A-C) we show 3 simulations in which h_{ac} is increased compared to the intermediate-friction case by increasing μ (pink), increasing D_{RS} (yellow) or decreasing b (turquoise) while keeping t_s constant. Figures S13 and S14(D-E) show simulations in which both t_s and h_{ac} are increased by increasing f^*(pink) or θ_{ini} (yellow). Figures S13 and S14(F) also show a case (turquoise) in which both t_s and h_{ac} are kept the same as in the intermediate-friction reference case but t_{ac} is delayed due to the decreased hydraulic diffusivity α which controls how fast the slipping zone expands during Stage 2. In all cases, the onset of Stage 3 is delayed compared to the intermediate-friction reference case. Thus, parameters μ, D_{RS}, b, t_s and α have a primary control on the onset of Stage 3 observed in all simulations shown in this work.

As for the amplitude and slope of the slip acceleration, four parameters - f^*, $a - b$, μ and α - have been identified to play a key role in controlling them as shown in Figures S15 to S19.

Table S1. Model parameters for the three cases presented in Figures 2-4 in the main text.

Properties	Symbol	Low Friction	Intermediate Friction	High Friction
Total fault length [m]	x_{tot}	250	250	250
Frictional interface length [m]	x_{fr}	200	200	200
Initial shear stress [MPa]	τ_{ini}	2.15	2.15	2.15
Initial normal stress [MPa]	σ_{ini}	4.00	4.00	4.00
Initial coefficient of friction	f_{ini}	0.5375	0.5375	0.5375
Reference coefficient of friction	f^{*}	0.4815	0.5500	0.6000
Reference slip rate [m/s]	V^{*}	10^{-6}	10^{-6}	10^{-6}
Direct effect frictional parameter	a	0.01500	0.01125	0.01125
Evolutionary effect frictional parameter	b	0.01600	0.01600	0.01600
Critical slip distance [μm]	D_{RS}	16.75	16.75	16.75
Hydraulic diffusivity [m^2/s]	α	0.04	0.20	0.85
Initial state variable [s]	θ_{ini}	1.21e12	2.38e12	7.00e12
Shear modulus [GPa]	μ	10	10	10
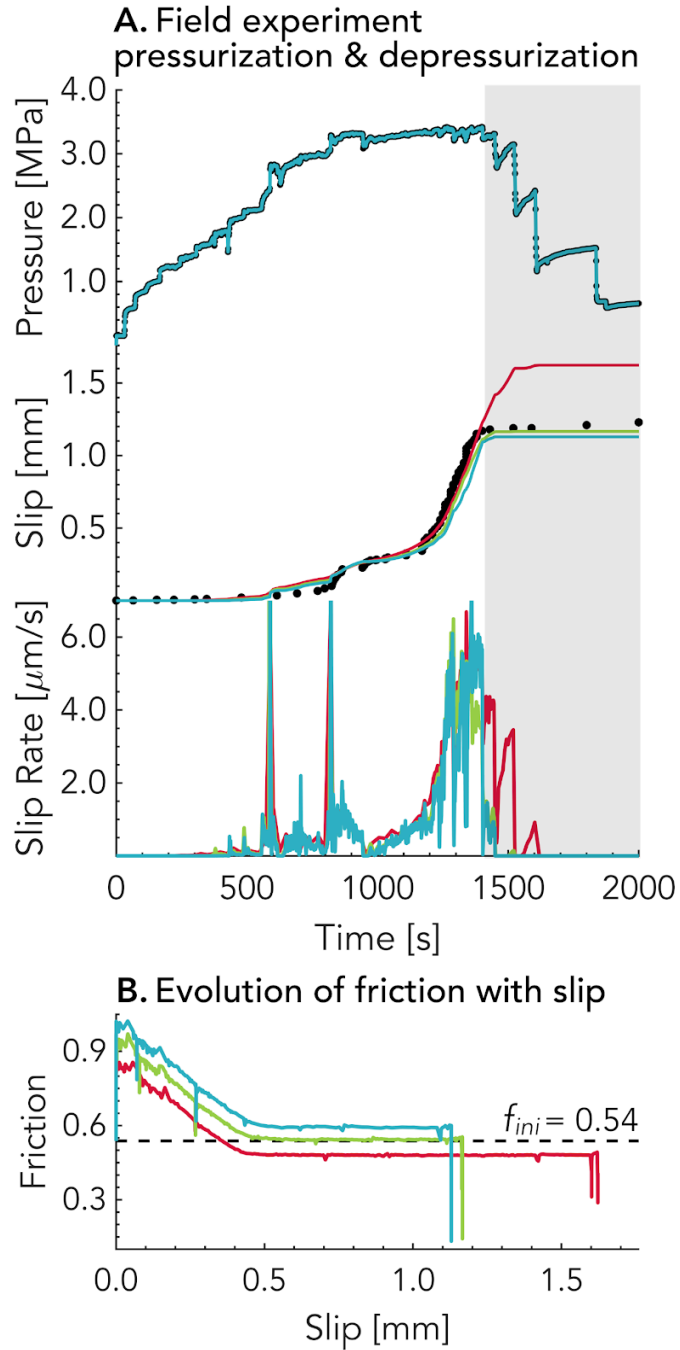
Figure S1. Temporal evolution of pore pressure, slip and slip rate and evolution of friction as a function of slip as in Figure 2AB in the main text but for the exact pressure history. The simulated slip rate is similar but noisier and harder to interpret.
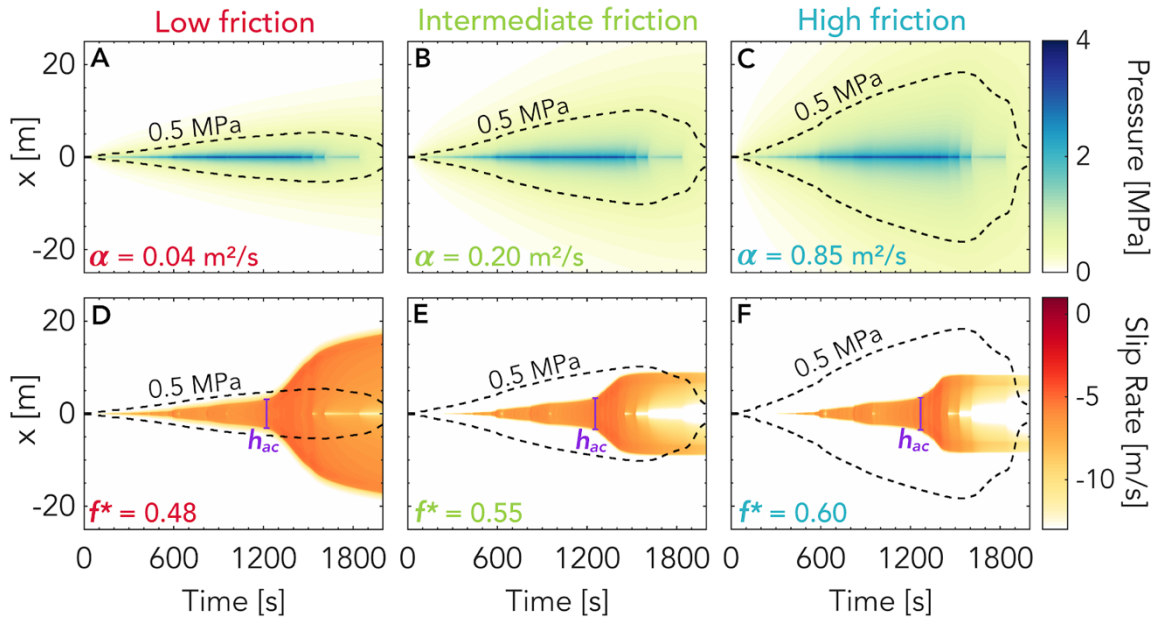
Figure S2. Spatial and temporal evolution of pore pressure and slip as Figure 3 in the main text but for the exact pressure history as in Figure S1 and including the depressurization stage.
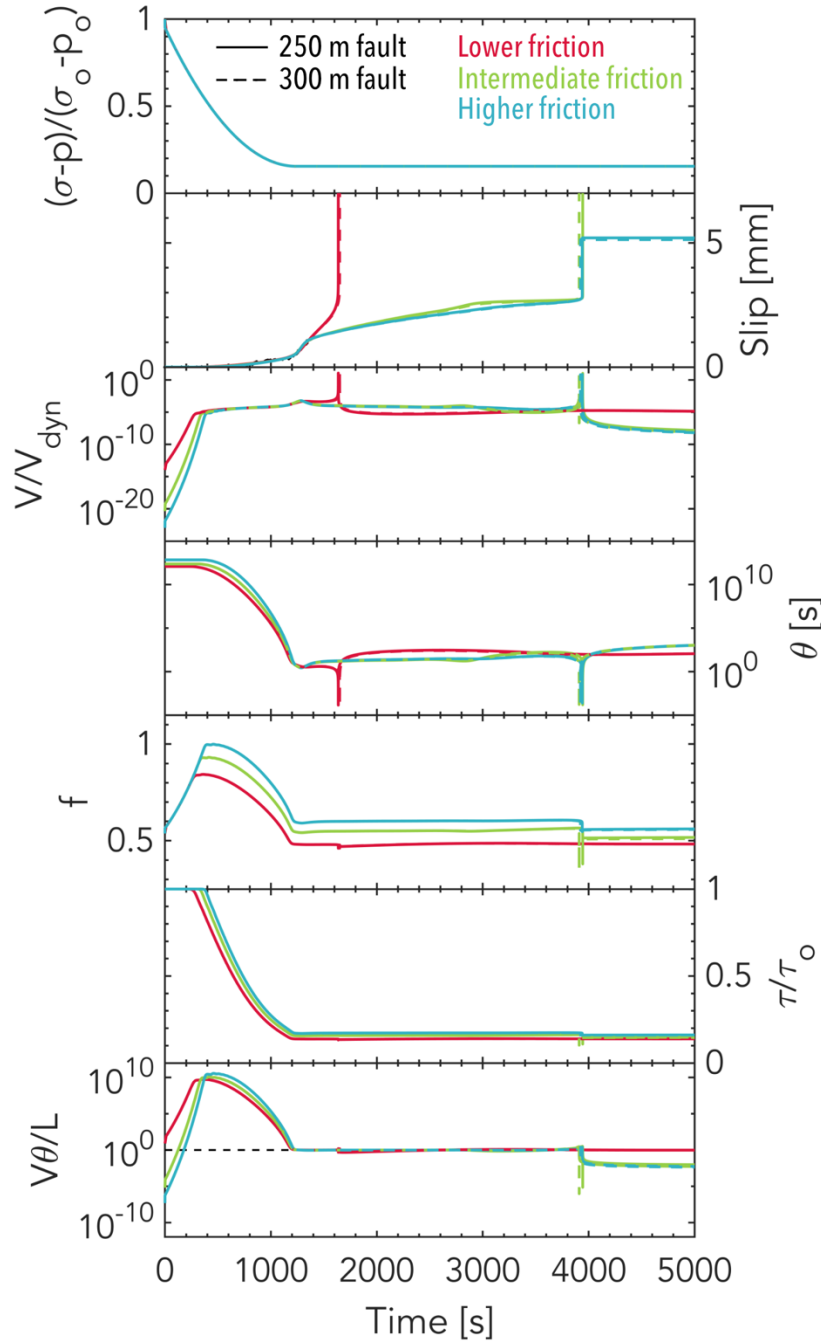
Figure S3. Temporal evolution of several quantities at the injection site for the prolonged injection simulations (Figure 4) with domain sizes of 250 m (solid lines) and 300 m (dashed lines). From top to bottom: the normalized effective normal stress, slip, normalized slip rate ($V_{dyn} = 10^{-2}$ m/s), state variable, friction coefficient, normalized shear stress and closeness to steady state at the injection site. Changing the domain size slightly changes the timing of the dynamic events but not the overall behavior.
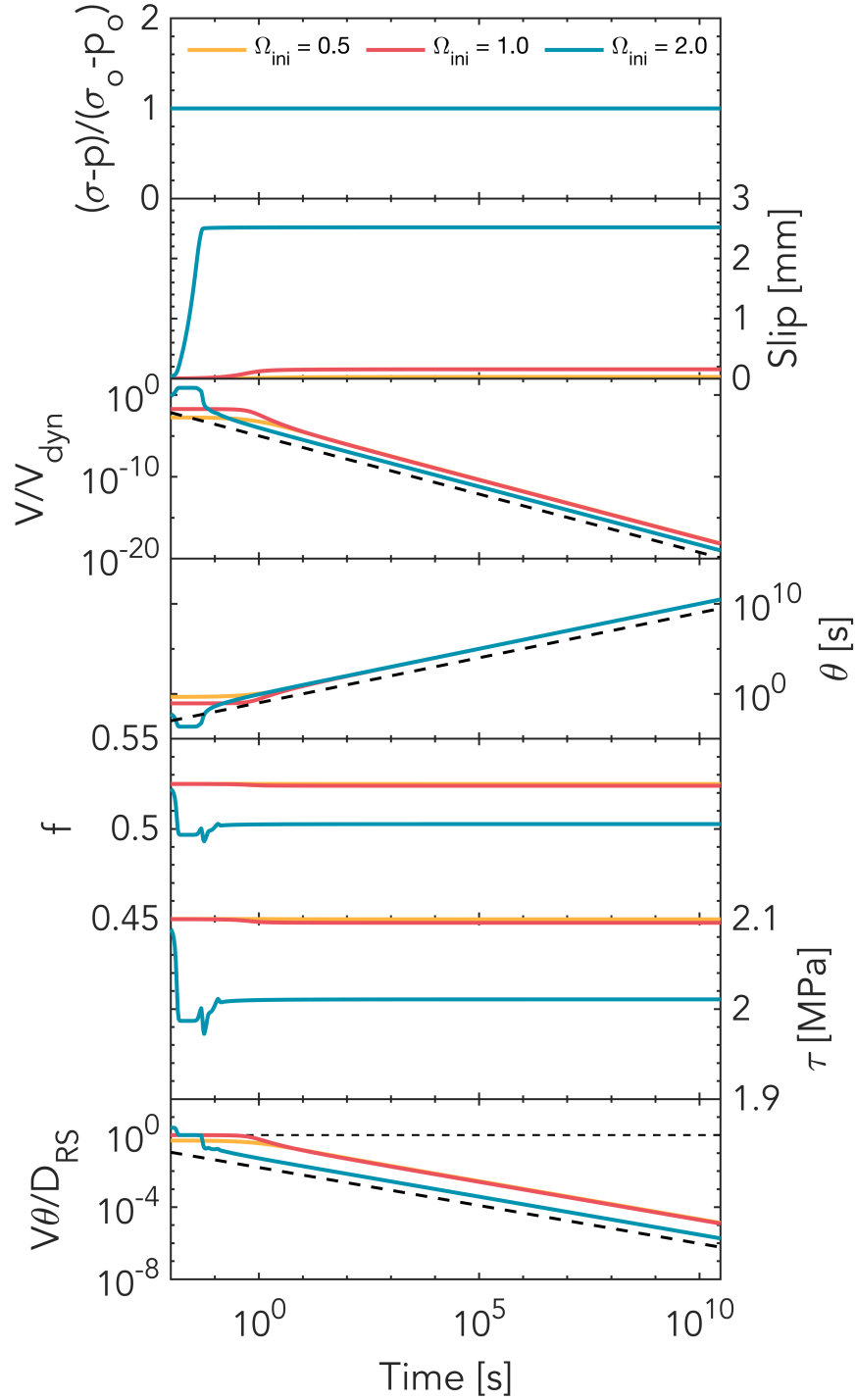
Figure S4. Simulations that illustrate long-term fault healing in the absence of slip, with $f^* = 0.550$, $f_{ini} = 0.525$, $a = 0.011$, and $b = 0.016$, varying the initial closeness to steady state ($\Omega_{ini} = V_{ini}\theta_{ini}/D_{RS}$). No matter what the initial values are, all cases eventually undergo a logarithmic decrease in slip rate and an increase in state variable with time. Note that the time axis is logarithmic. The thick dashed lines indicate the slopes discussed in the Text S1.
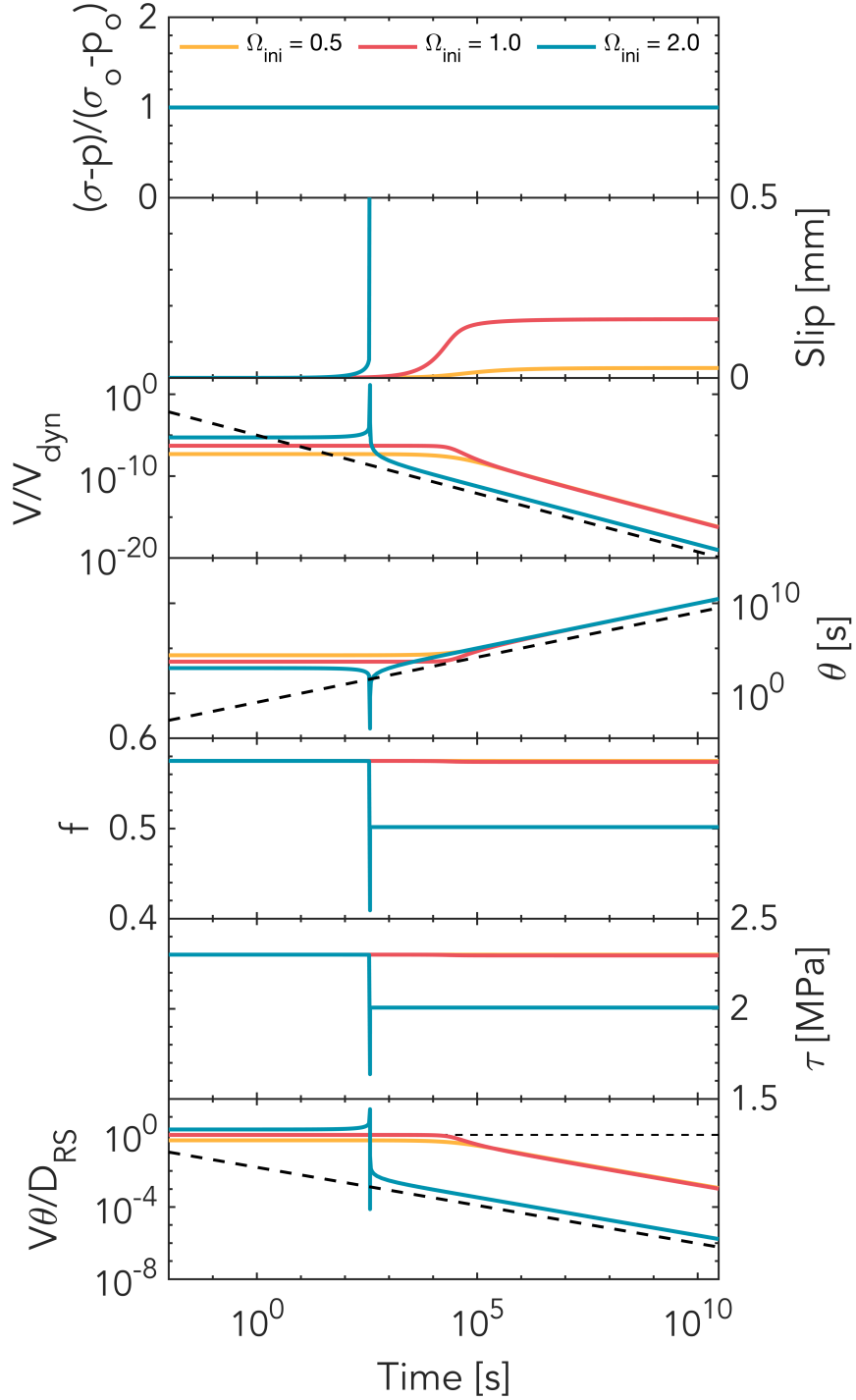
Figure S5. Simulations that illustrate long-term fault healing in the absence of slip, with $f^* = 0.550$, $f_{ini} = 0.575$, $a = 0.011$, and $b = 0.016$, varying the initial closeness to steady state ($\Omega_{ini} = V_{ini}\theta_{ini}/D_{RS}$). No matter what the initial values are, all cases eventually undergo a logarithmic decrease in slip rate and an increase in state variable with time, even the initially above steady-state case which experiences a run-away earthquake a few minutes into the simulation. Note that the time axis is logarithmic. The thick dashed lines indicate the slopes discussed in Text S1.
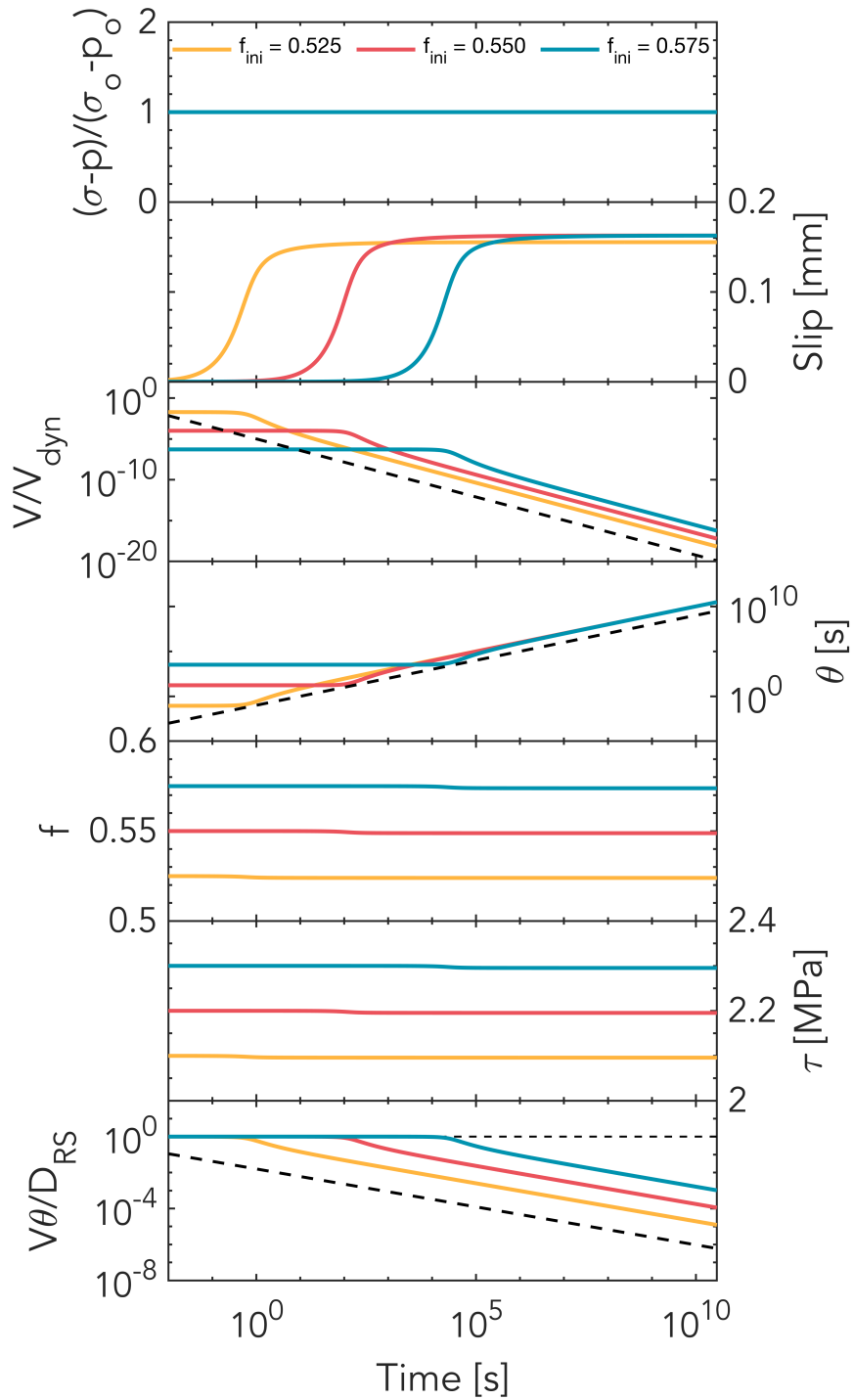
Figure S6. Simulations that illustrate long-term fault healing in the absence of slip, with $f^* = 0.550$, $\Omega_{ini} = 1$, $a = 0.011$, and $b = 0.016$, varying the initial friction coefficient, f_{ini}. No matter what the initial values are, all cases eventually undergo a logarithmic decrease in slip rate and an increase in state variable with time. Note that the time axis is logarithmic. The thick dashed lines indicate the slopes discussed in Text S1.
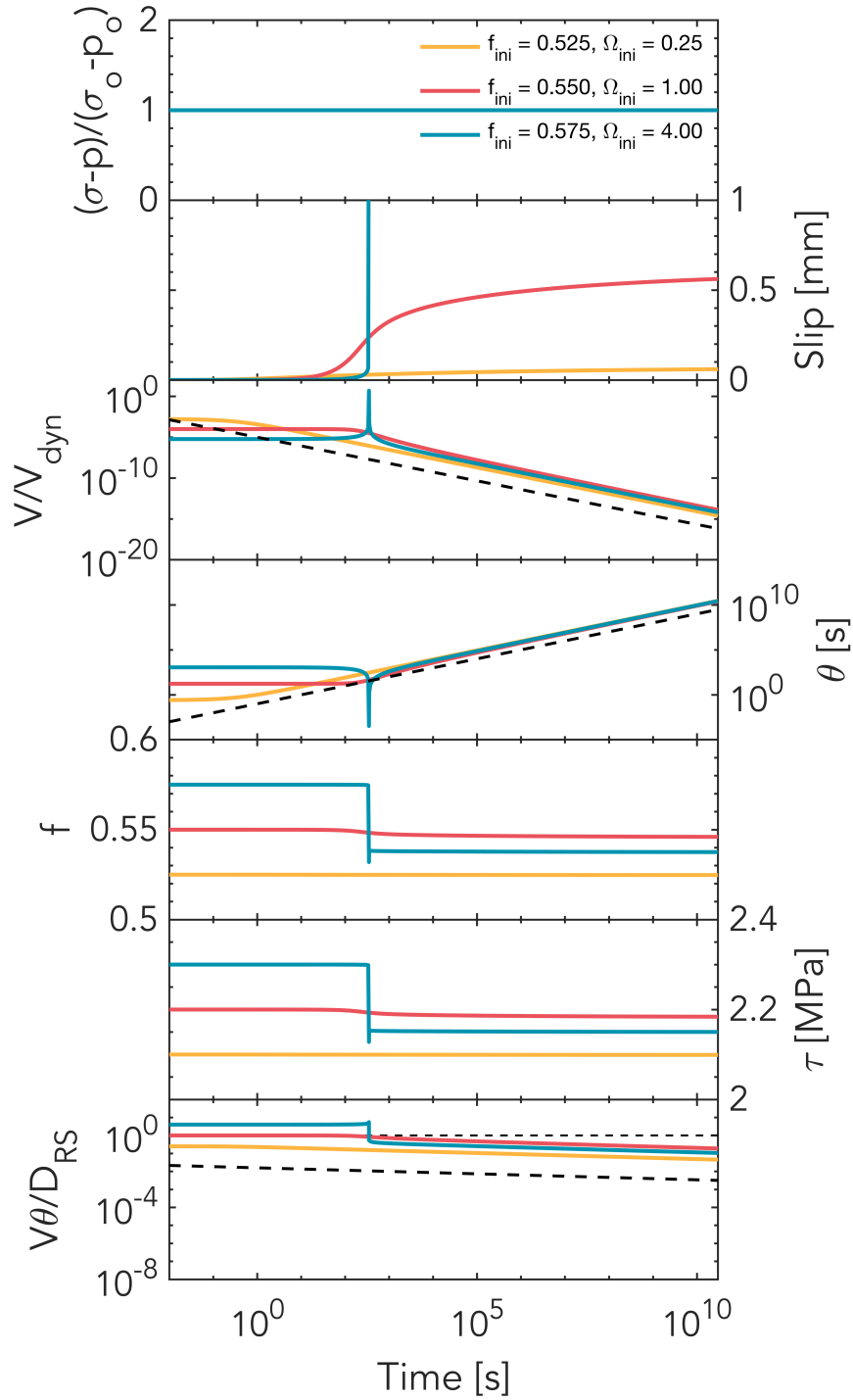
Figure S7. Simulations that illustrate long-term fault healing in the absence of slip, with $f^* = 0.550$, $a = 0.015$, and $b = 0.016$, varying the initial closeness to steady state ($\Omega_{ini} = V_{ini}\theta_{ini}/D_{RS}$) and initial friction coefficient f_{ini}. No matter what the initial values are, all cases eventually undergo a logarithmic decrease in slip rate and an increase in state variable with time, even the initially above steady-state case which experiences a run-away earthquake a few minutes into the simulation. Note that the time axis is logarithmic. The thick dashed lines indicate the slopes discussed in Text S1.

11
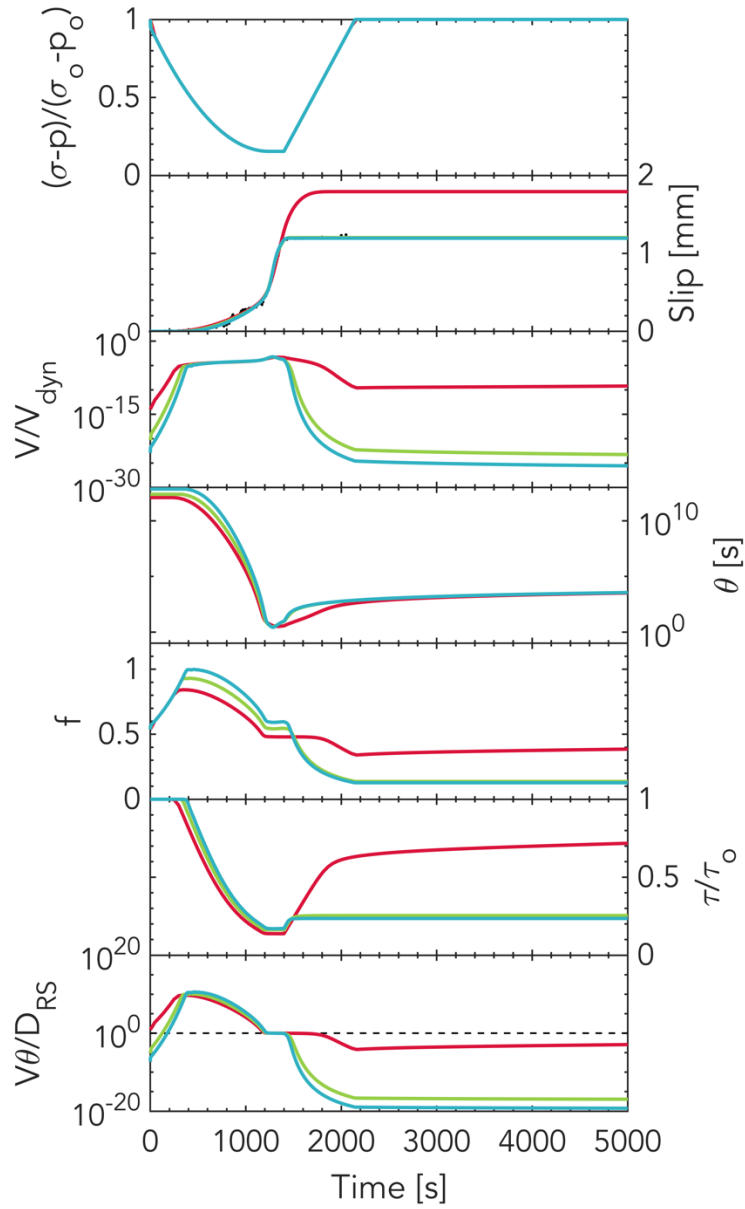
Figure S8. Simulated temporal evolution of several quantities at the injection site for the cases of Figure 2A in the main text. From top to bottom: the normalized effective normal stress, slip, normalized slip rate ($V_{dyn} = 10^{-2}$ m/s), state variable, friction coefficient, normalized shear stress and closeness to steady state at the injection site. Note that no earthquakes occur in these simulations as opposed to cases in which the pressure is kept constant at the injection site (Figure 4 in the main text).
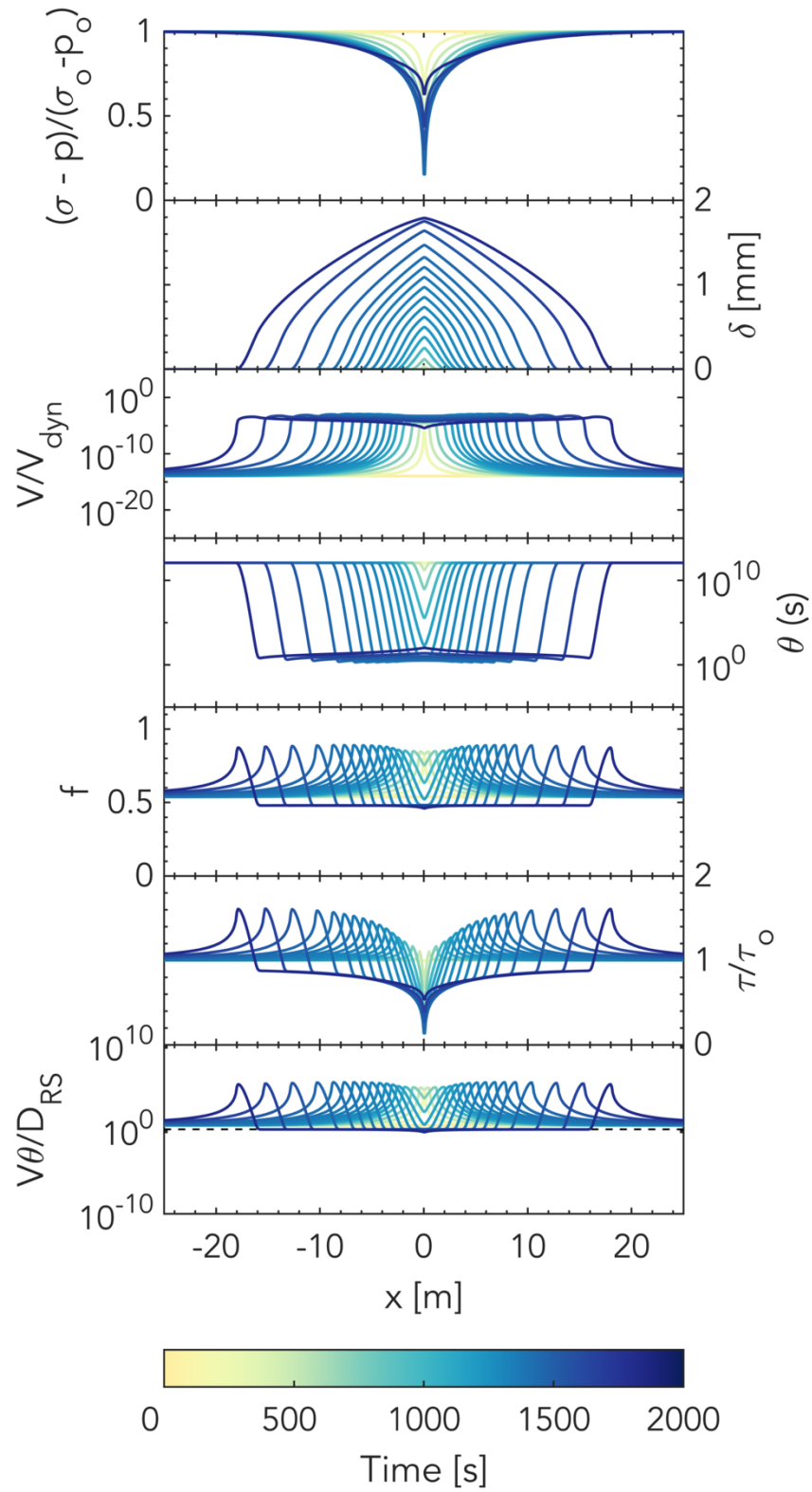
Figure S9. Spatial and temporal evolution of the same quantities as in Fig. S8 for the low-friction case (plotted every 2000 time steps).
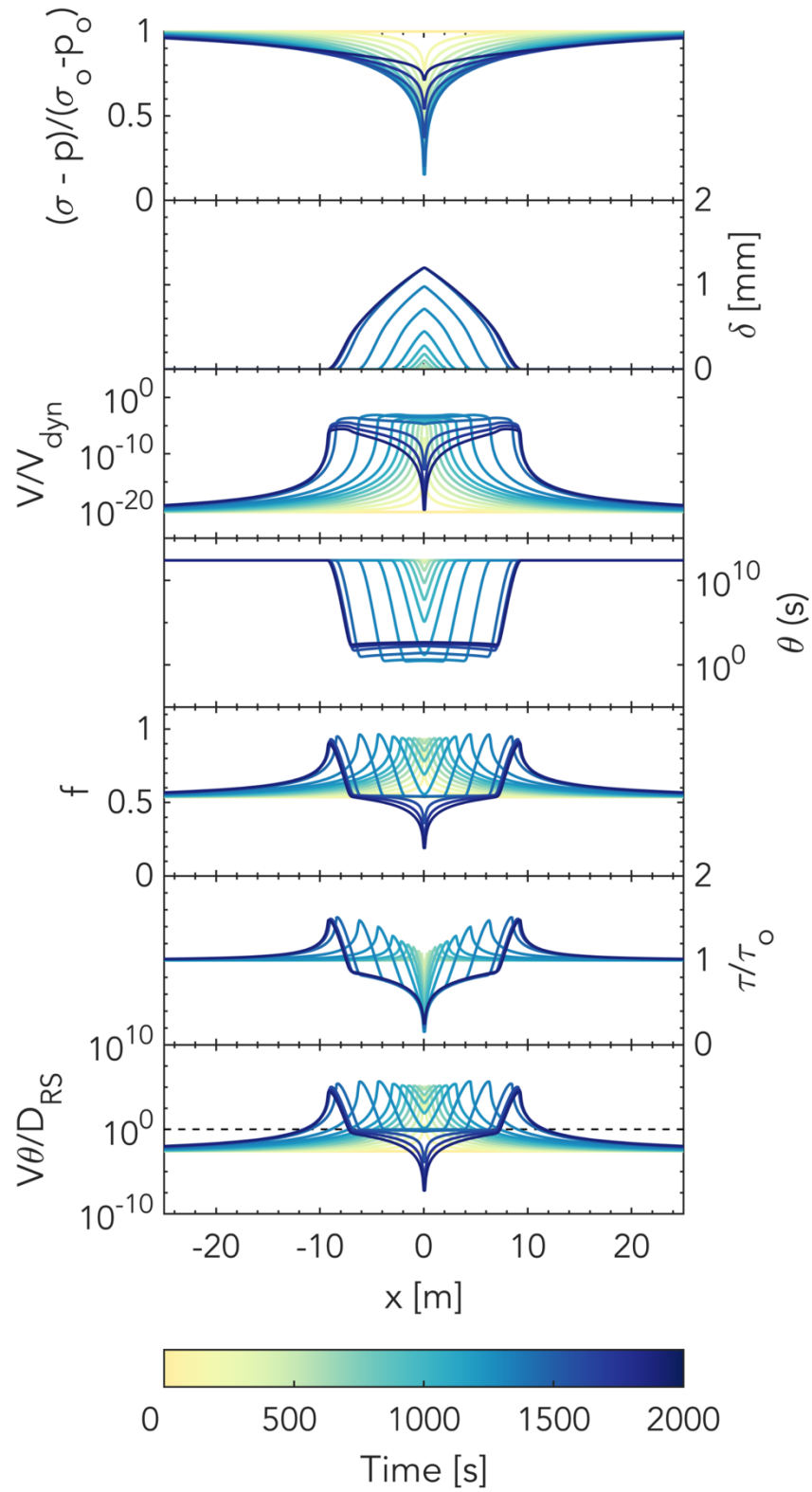
Figure S10. Spatial and temporal evolution of the same quantities as in Fig. S8 for the intermediate-friction case (plotted every 6000 time steps).
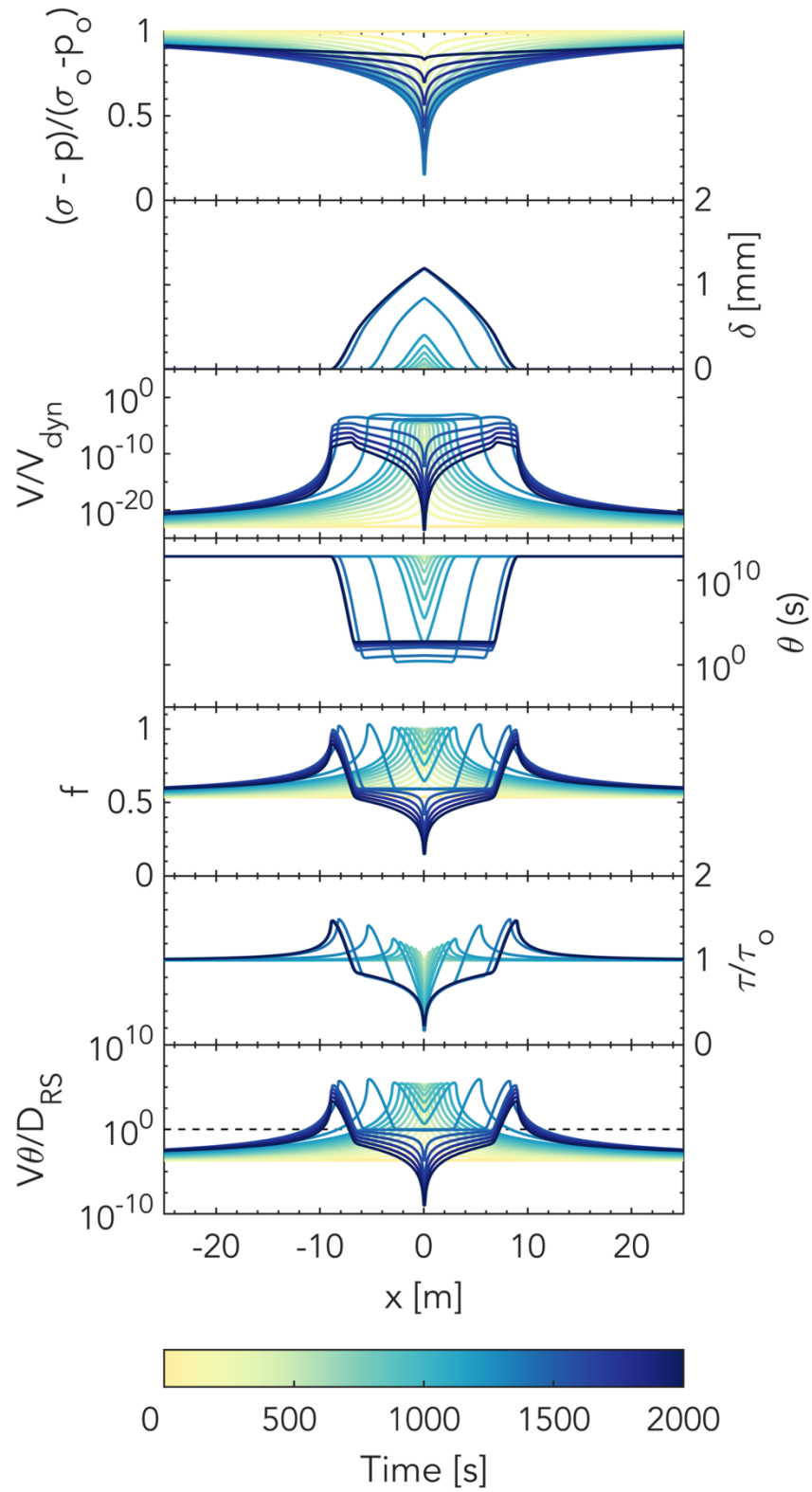
Figure S11. Spatial and temporal evolution of the same quantities as in Fig. S8 for the high-friction case (plotted every 20000 time steps).
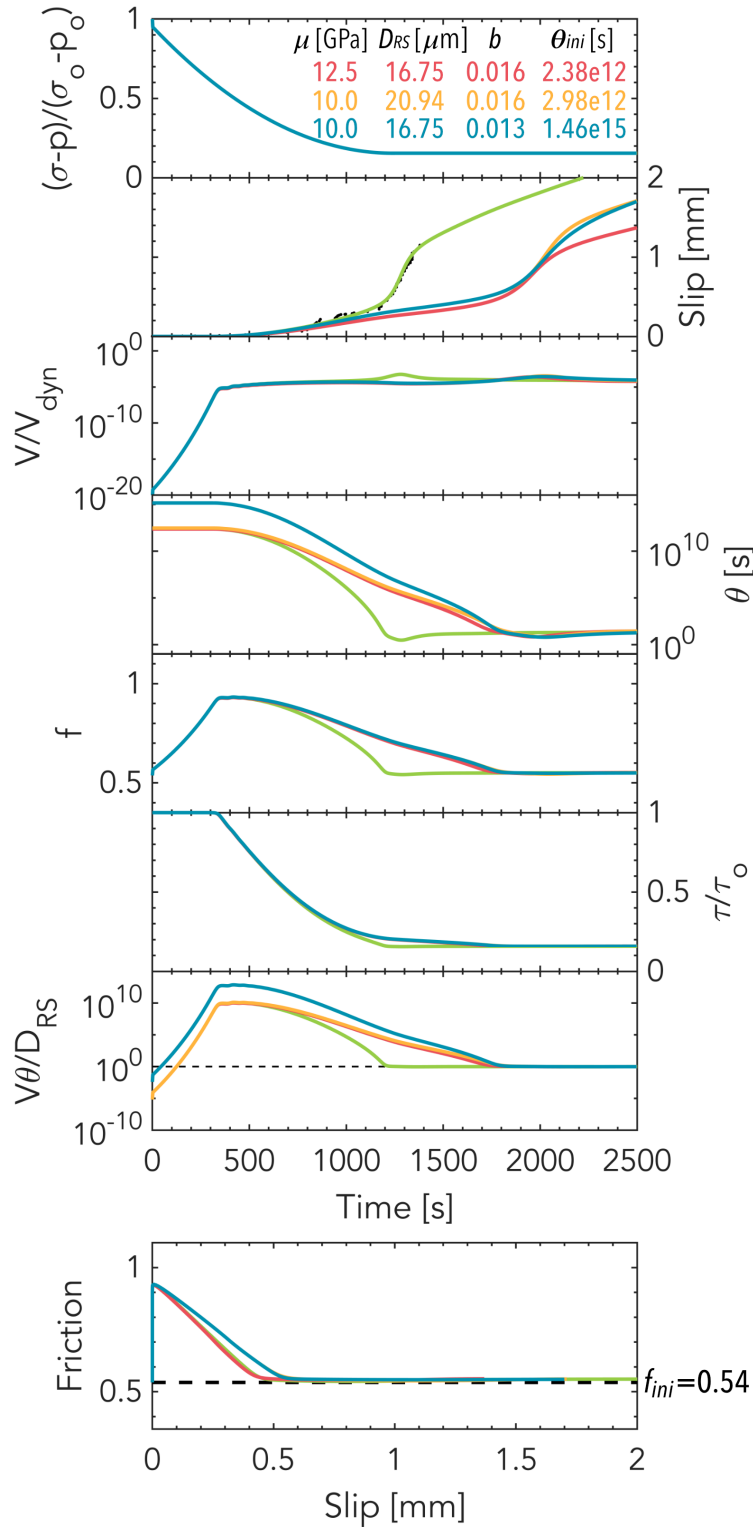
Figure S12. Temporal evolution of quantities at the injection site and friction vs. slip for prolonged injection but for cases in which the onset of Stage 3 is delayed by increasing μ (pink), increasing D_{RS} (yellow) or decreasing b (turquoise) compared to the intermediate-friction reference case (green). Note the delay in the transient acceleration compared to the reference case. Parameter values modified from the intermediate-friction scenario are listed at the top right corner.
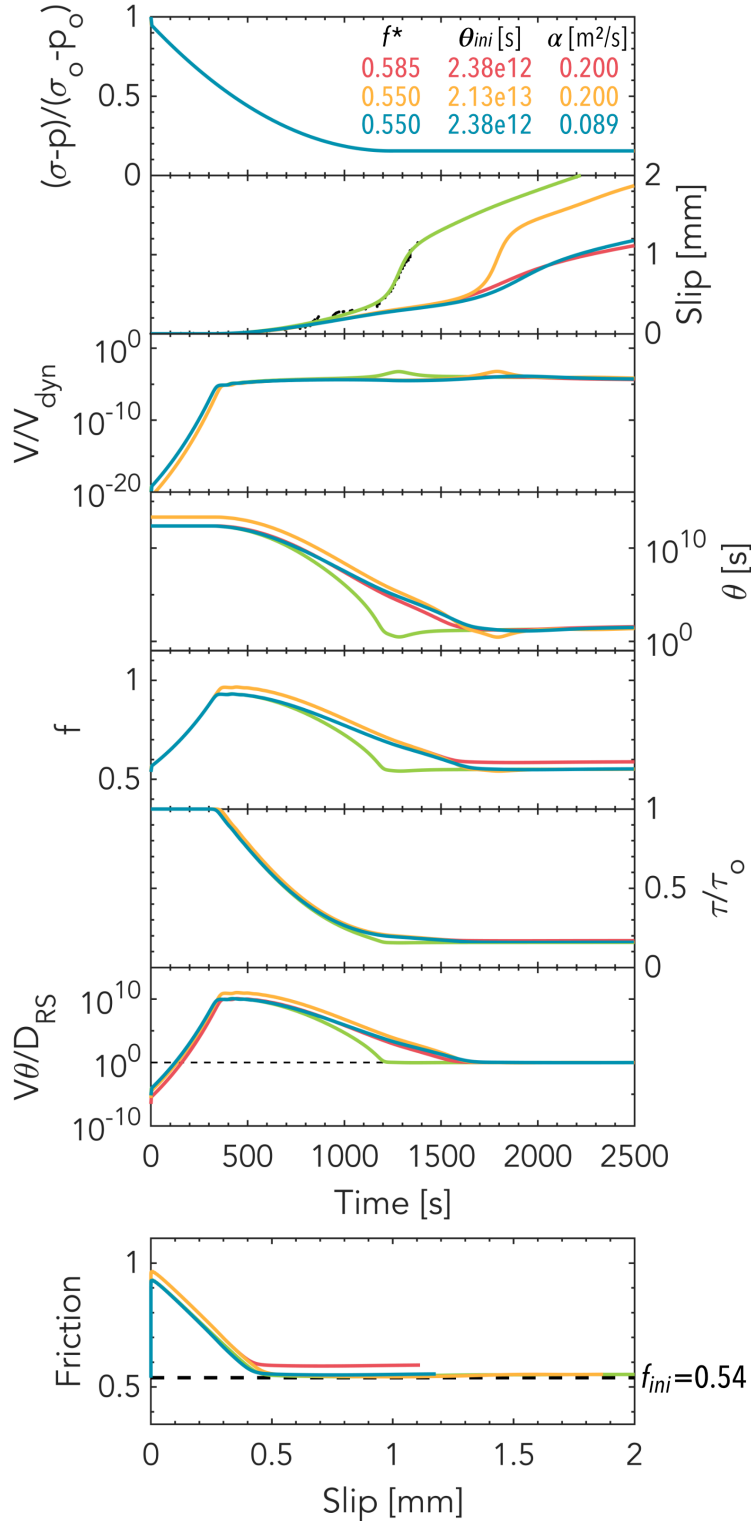
Figure S13. Temporal evolution of quantities at the injection site and friction vs. slip for prolonged injection but for cases in which the onset of Stage 3 is delayed by increasing f^* (pink), increasing θ_{ini} (yellow) or decreasing α (turquoise) compared to the intermediate-friction reference case (green). Note the delay in the transient acceleration compared to the reference case. Parameter values modified from the intermediate-friction scenario are listed at the top right corner.
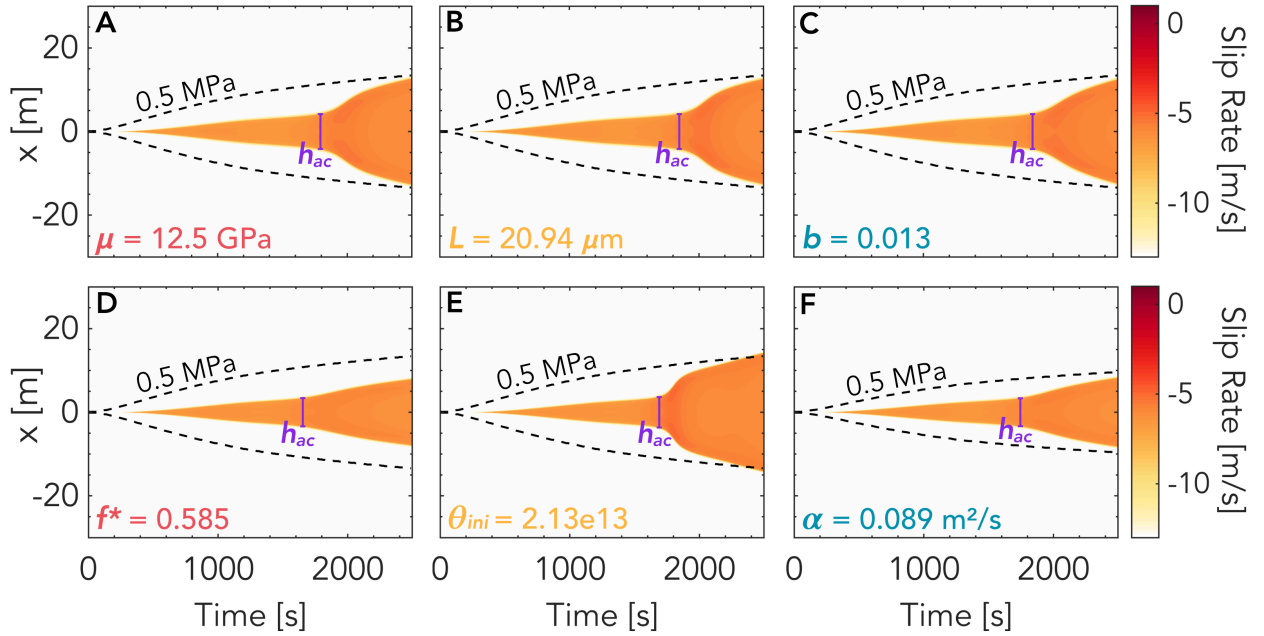
**Figure S14.** Spatial and temporal evolution of slip rate for the modified prolonged injection cases shown in Figures S12 and S13 in which the onset of Stage 3 is delayed by (A) increasing μ, (B) increasing D_{RS}, (C) decreasing b, (D) increasing f^*, (E) increasing θ_{ini}, (F) decreasing hydraulic diffusivity α. Note that h_{ac} provides a good estimate of the extent of the sliding region before the onset of Stage 3 in all these cases.
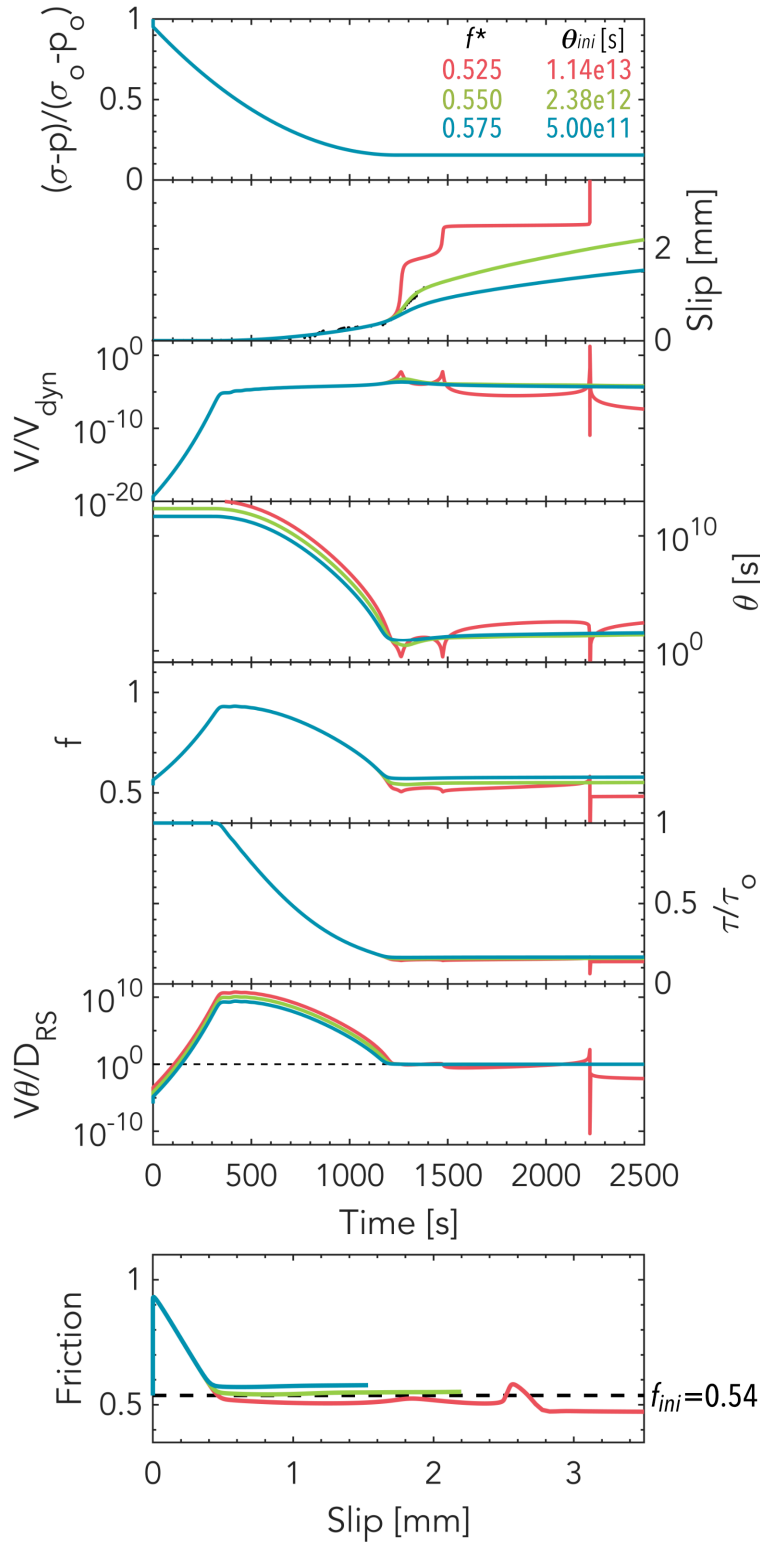
Figure S15. Temporal evolution of quantities at the injection site and friction vs slip of 2 cases showing the effect of varying f^* while keeping f^p constant. Increasing f^* reduces the amplitude and slope of the transient acceleration. Parameter values modified from the intermediate-friction scenario are listed at the top right corner.
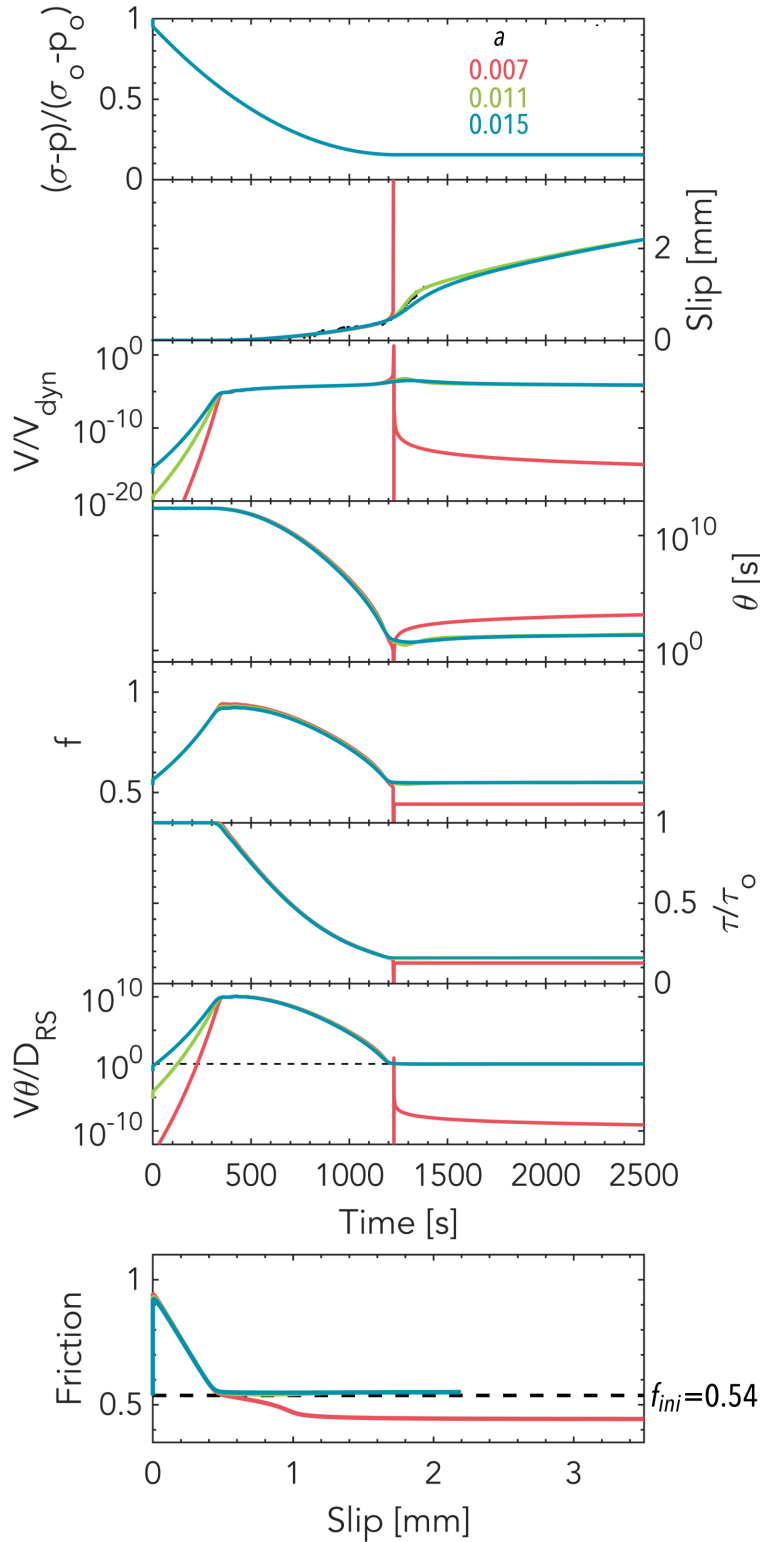
**Figure S16.** Temporal evolution of quantities at the injection site and friction vs slip of 2 cases showing the effect of varying a. Increasing a reduces the amplitude and slope of the transient acceleration. Parameter values modified from the intermediate-friction scenario (green) are listed at the top right corner.
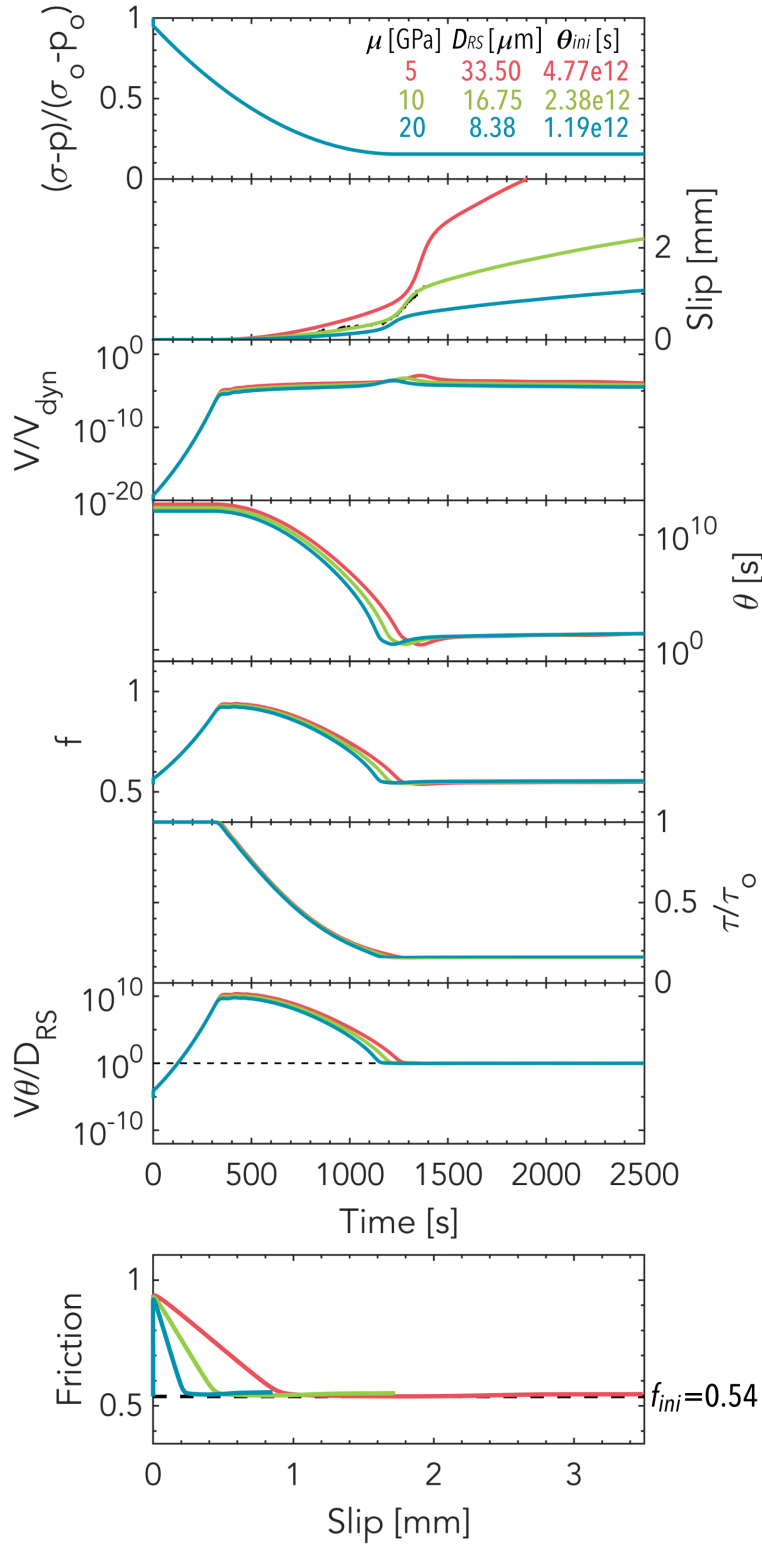
Figure S17. Temporal evolution of quantities at the injection site and friction vs slip of 2 cases showing the effect of varying μ while keeping h_{ac} and f^p constant. Increasing μ reduces the amplitude and slope of the transient acceleration. Parameter values modified from the intermediate-friction scenario (green) are listed at the top right corner.
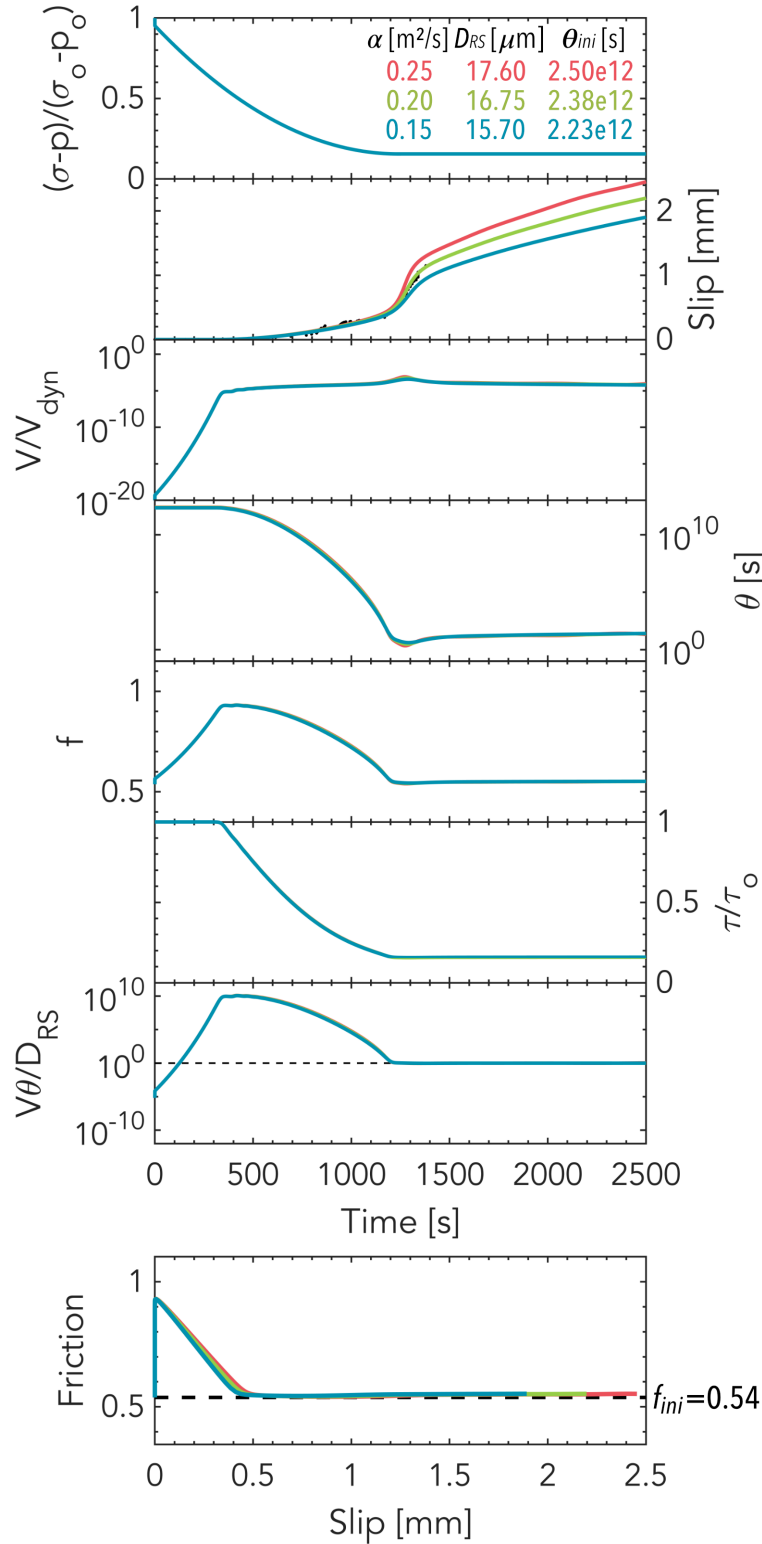
Figure S18. Temporal evolution of quantities at the injection site and friction vs slip of 2 cases showing the effect of varying α while keeping t_{ac} and f^p constant. Increasing α increases the amplitude and slope of the transient acceleration. Parameter values modified from the intermediate-friction scenario (green) are listed at the top right corner.
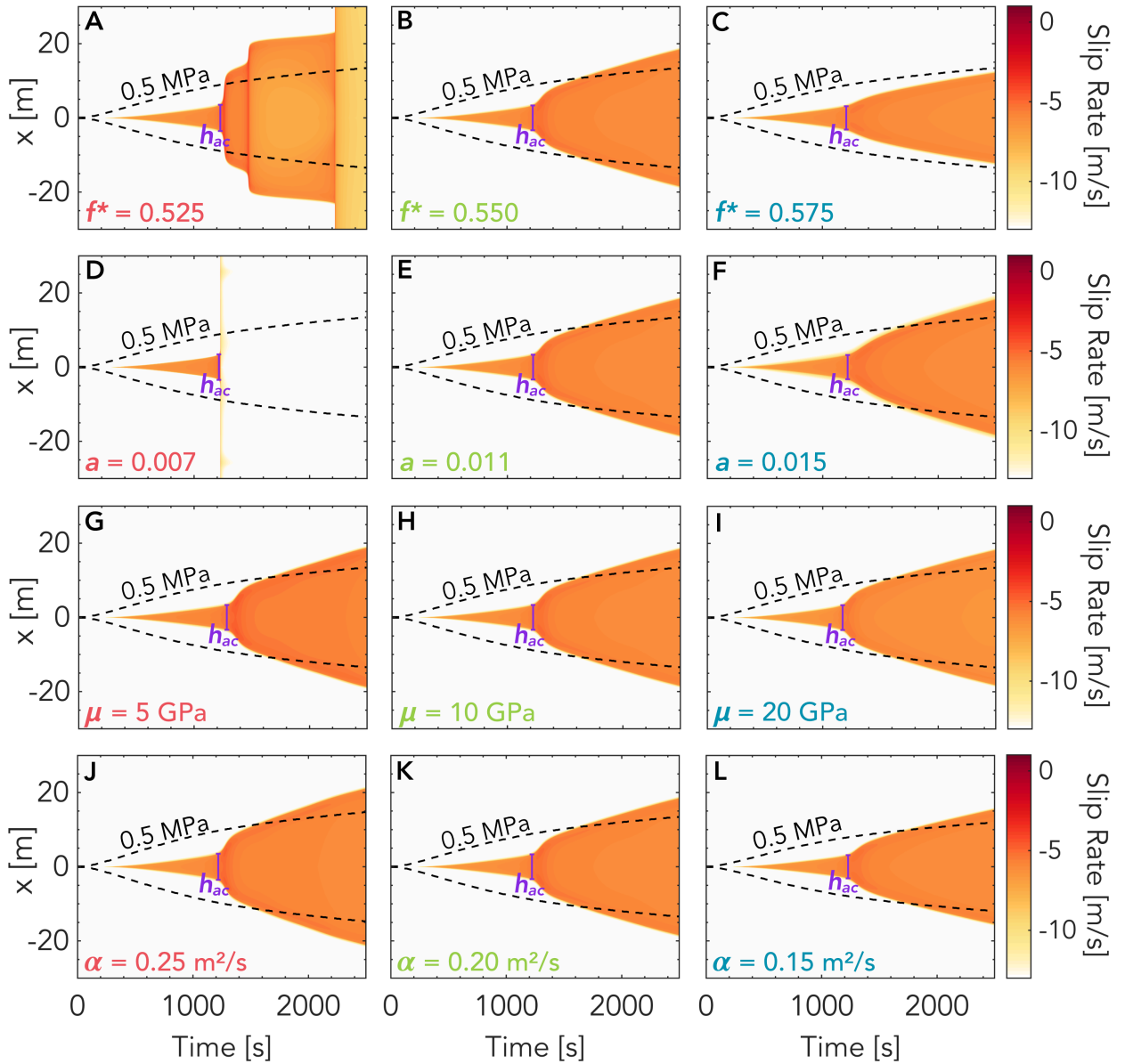
Figure S19. Spatial and temporal evolution of rate for the cases shown in Figures S15 − S18 in which the slope and/or amplitude of the transient acceleration is altered by varying (A,C) f^*, (D,F) a, (G,I) μ and (J,L) α. Panels B, E, H and K all show the reference intermediate-friction case for comparison purposes.
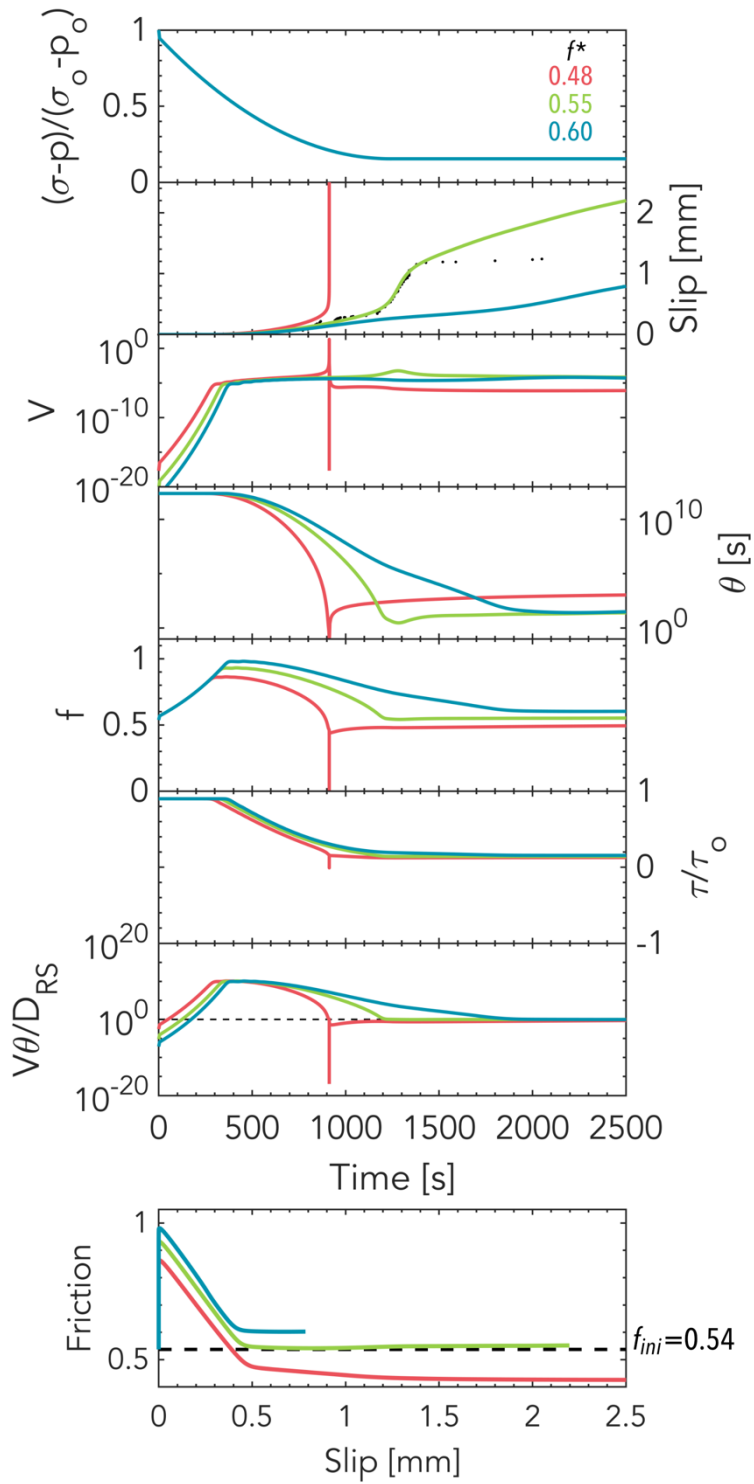
Figures S20. Simulated temporal evolution of several quantities at the injection site varying f^*, keeping all other parameter values as in the intermediate-friction scenario (green).
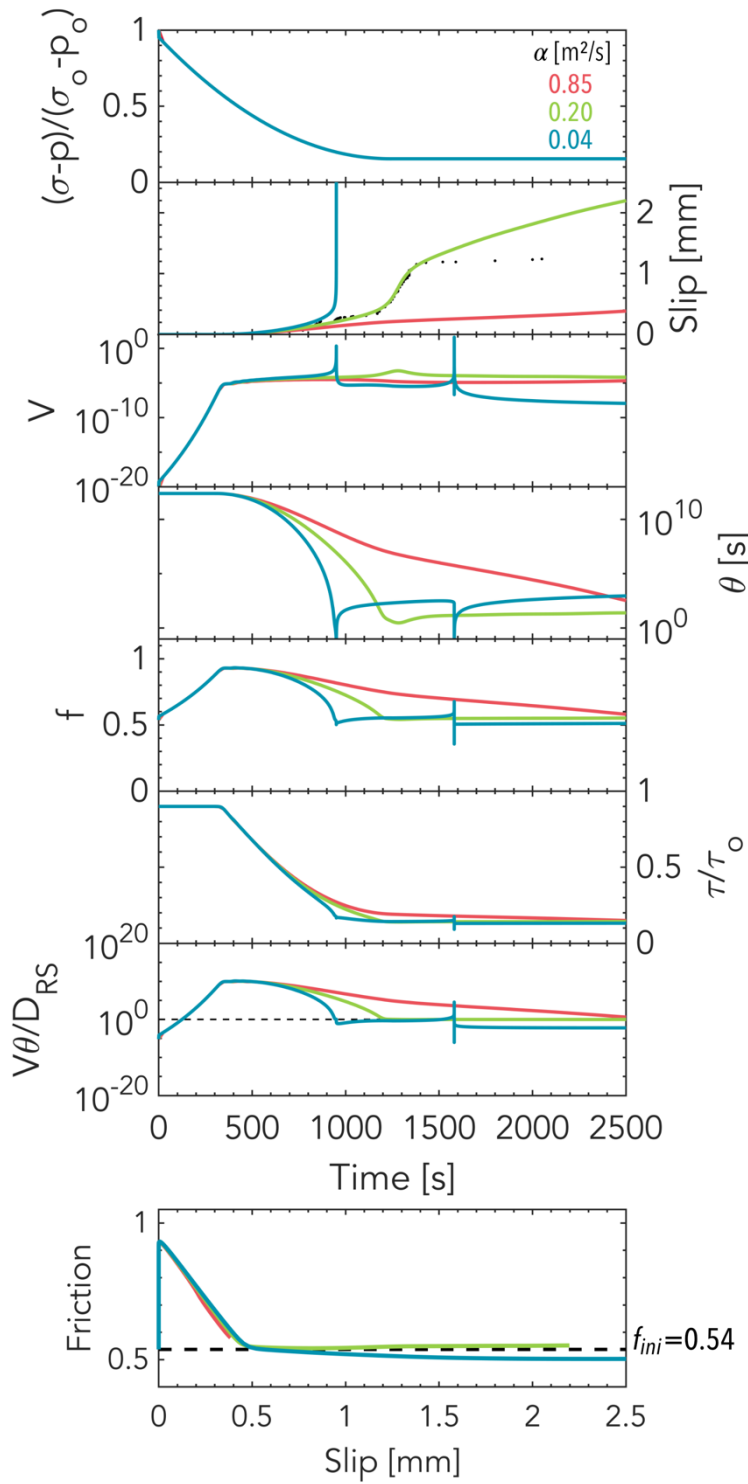
Figures S21. Simulated temporal evolution of several quantities at the injection site varying α, keeping all other parameter values as in the intermediate-friction scenario (green).
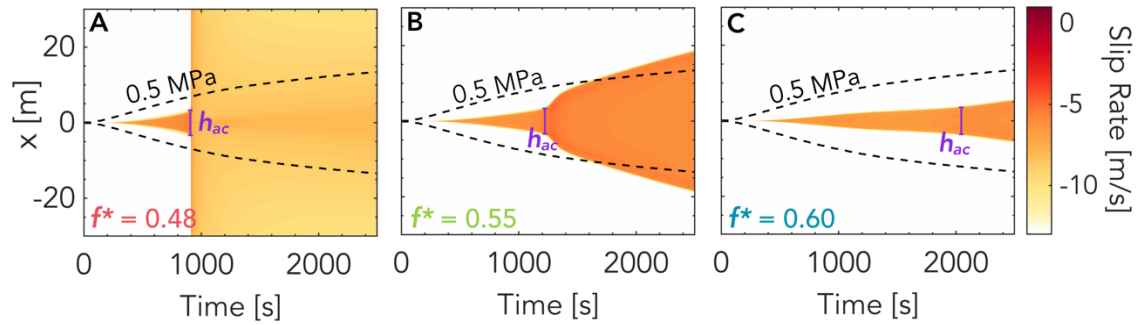
Figure S22. Spatial and temporal evolution of rate for the cases shown in Figures S20. Keeping everything else constant, varying f^* affects the spatial extent of the slipping zone compared to the pressurized zone.
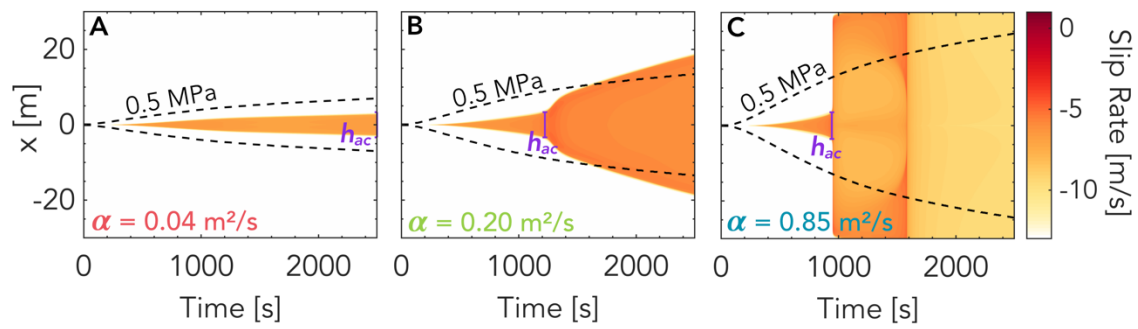

Figure S23. Spatial and temporal evolution of rate for the cases shown in Figures S21. Keeping everything else constant, varying α affects the spatial extent of the slipping zone.
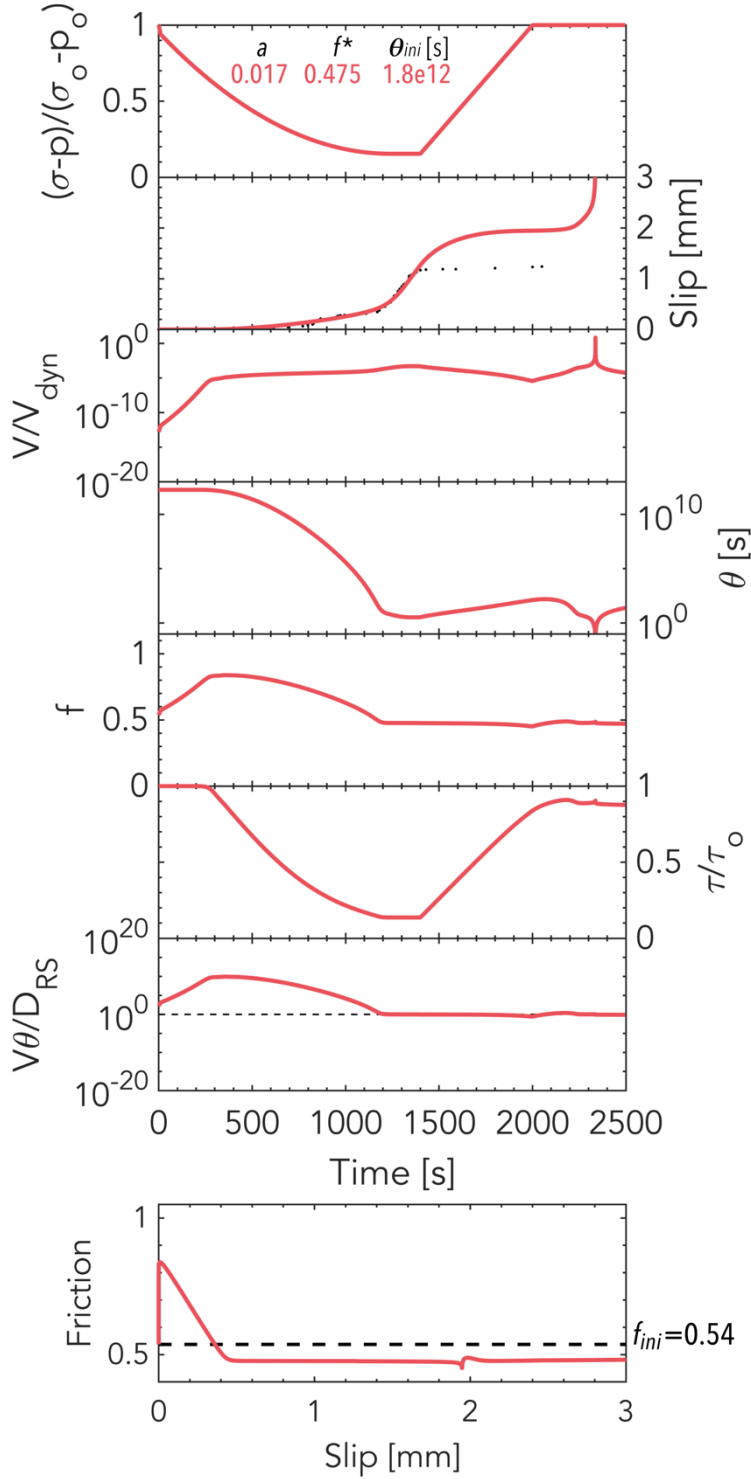
Figure S24: Simulated temporal evolution of several quantities at the injection site for a scenario similar to the low-friction case in the main text but for a slightly rate-strengthening fault with $a = 0.017$, $b = 0.016$, $f^* = 0.475$ and $\theta_{ini} = 1.8e12s$. Note that in this case an earthquake still nucleates after the injection stopped due to the relatively low residual friction f^r compared to f_{ini}.
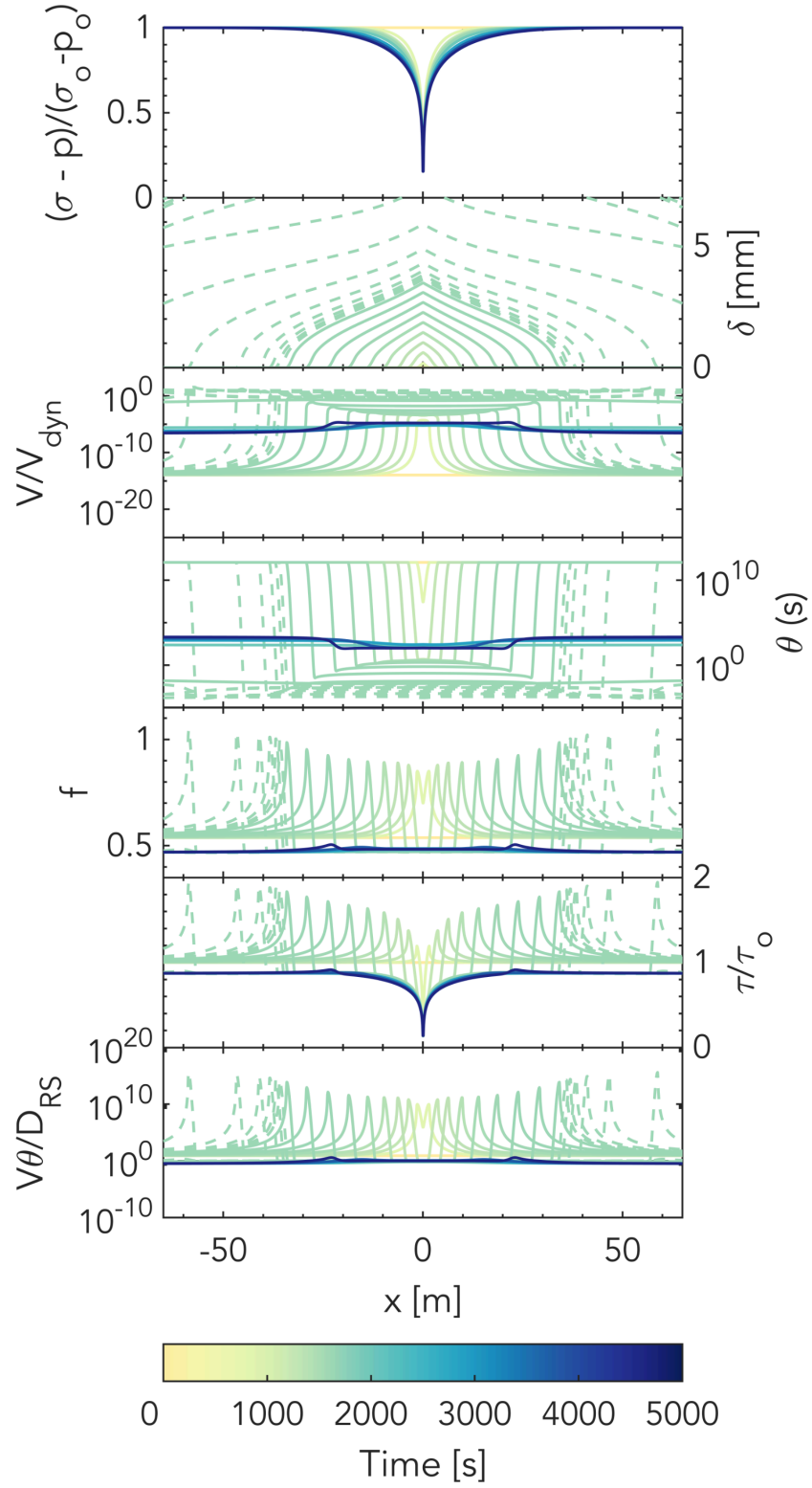
Figure S25. Spatial and temporal evolution for the low-friction prolonged injection case (plotted every 7000 time steps for $V < V_{dyn}$ and every 2000 time steps for $V > V_{dyn}$).
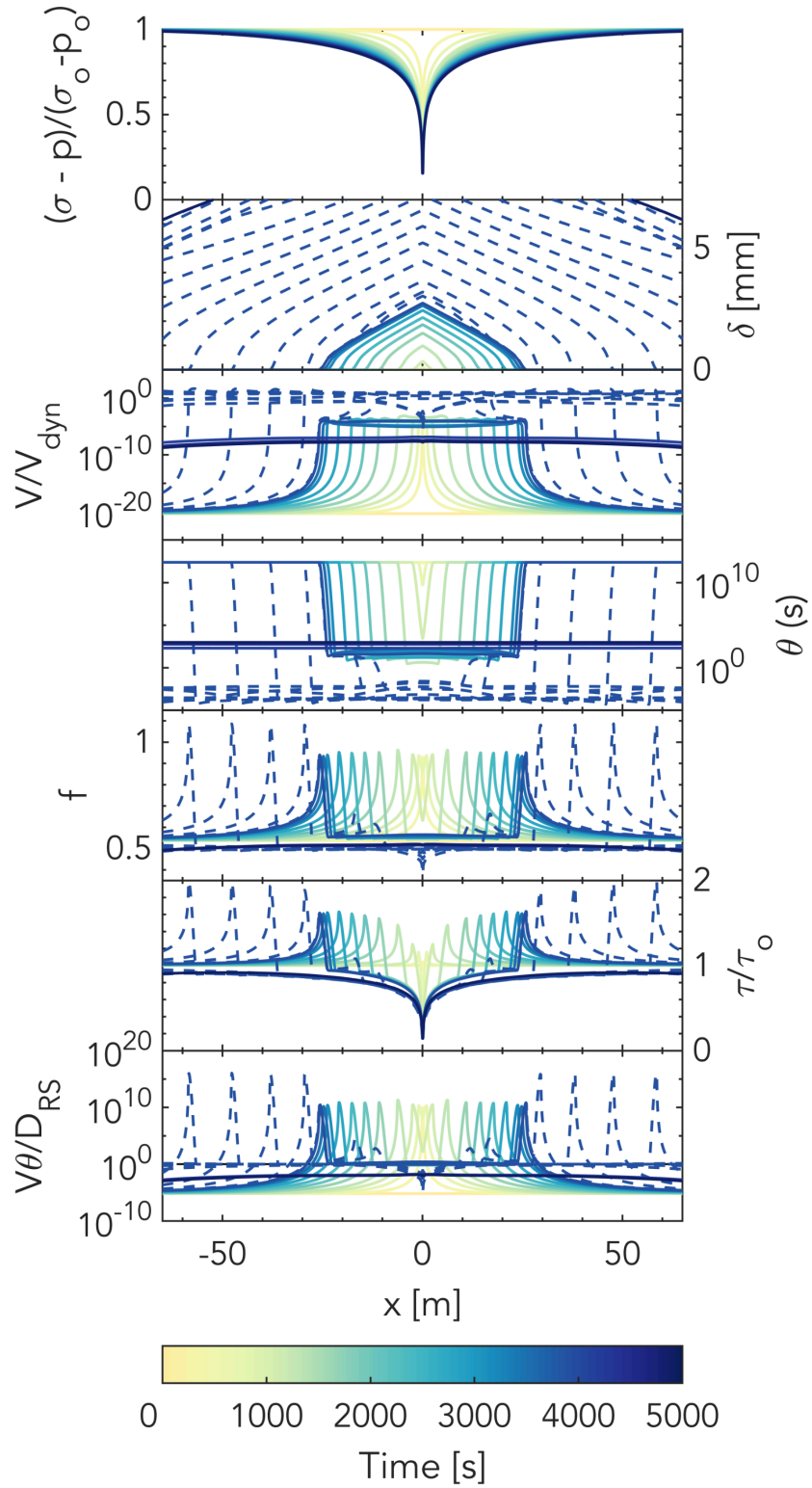
**Figure S26.** Spatial and temporal evolution for the intermediate-friction prolonged injection case (plotted every 15000 time steps for $V < V_{dyn}$ and every 1000 time steps for $V > V_{dyn}$).
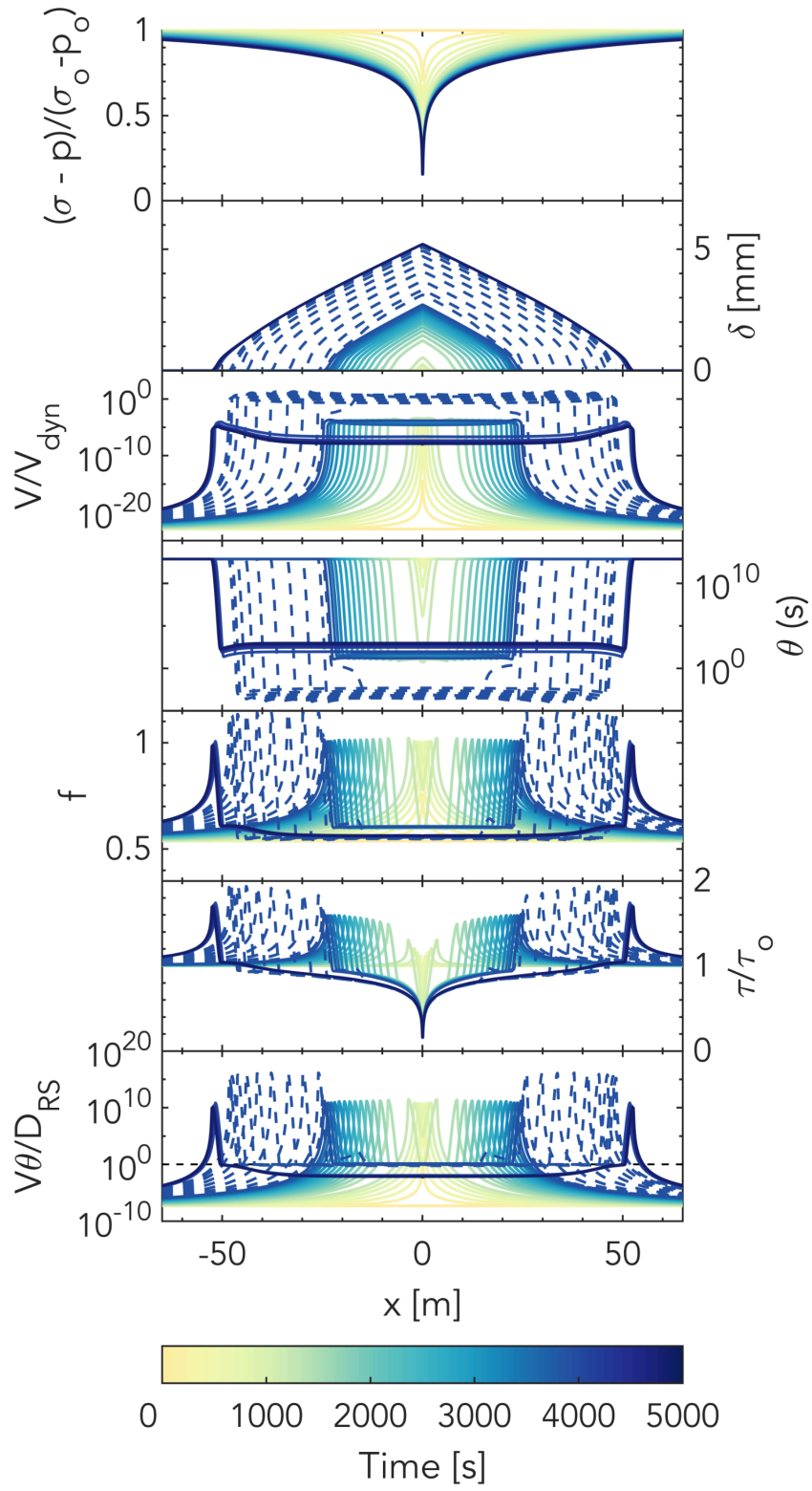
Figure S27. Spatial and temporal evolution for the high-friction prolonged injection case (plotted every 35000 time steps for $V < V_{dyn}$ and every 750 time steps for $V > V_{dyn}$).
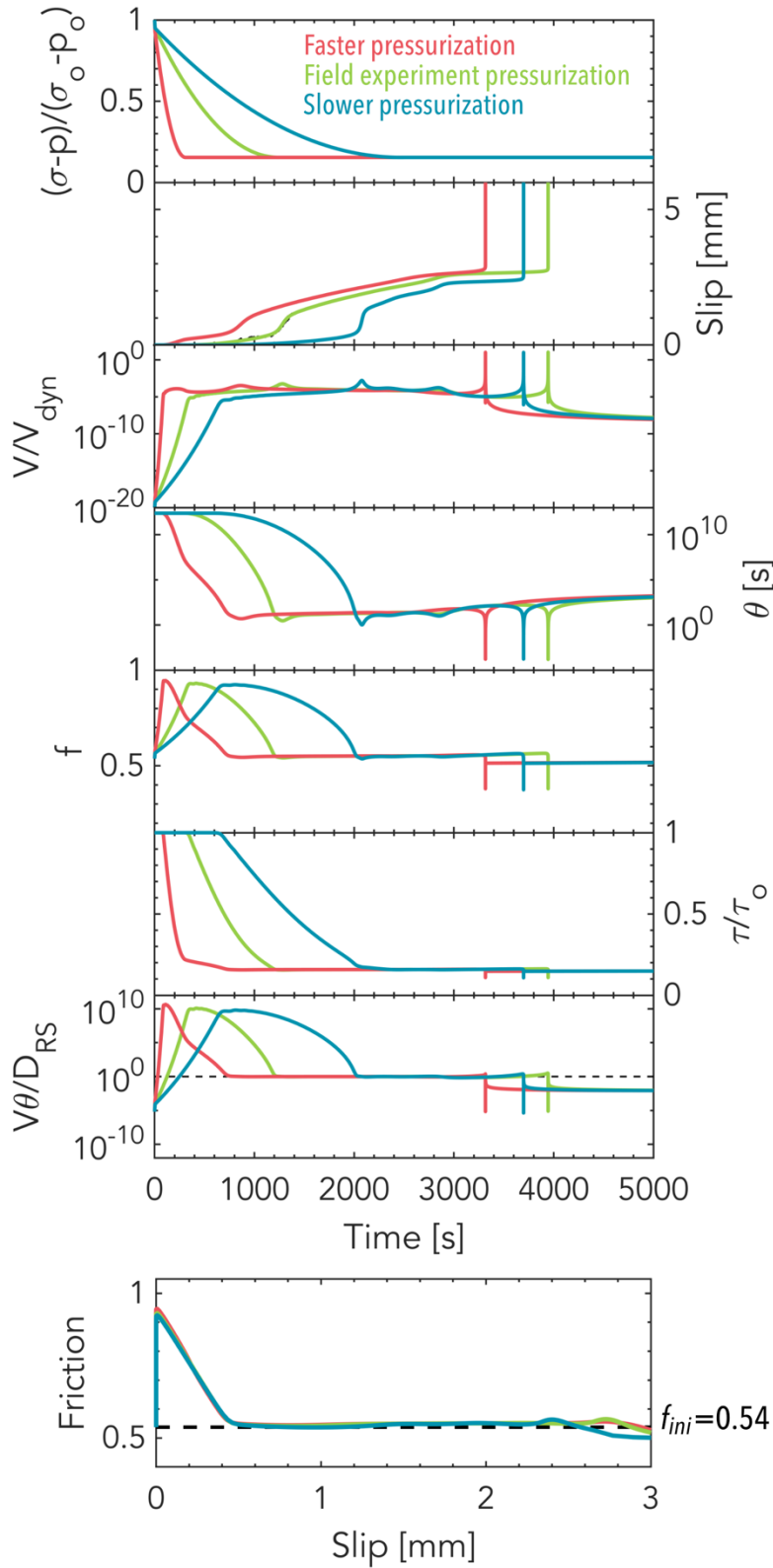
Figure S28. Effect of varying pressurization rate on the intermediate-friction case. The timing of events is altered but not the overall behavior, i.e., all simulations still show a transient acceleration followed by a run-away dynamic event.
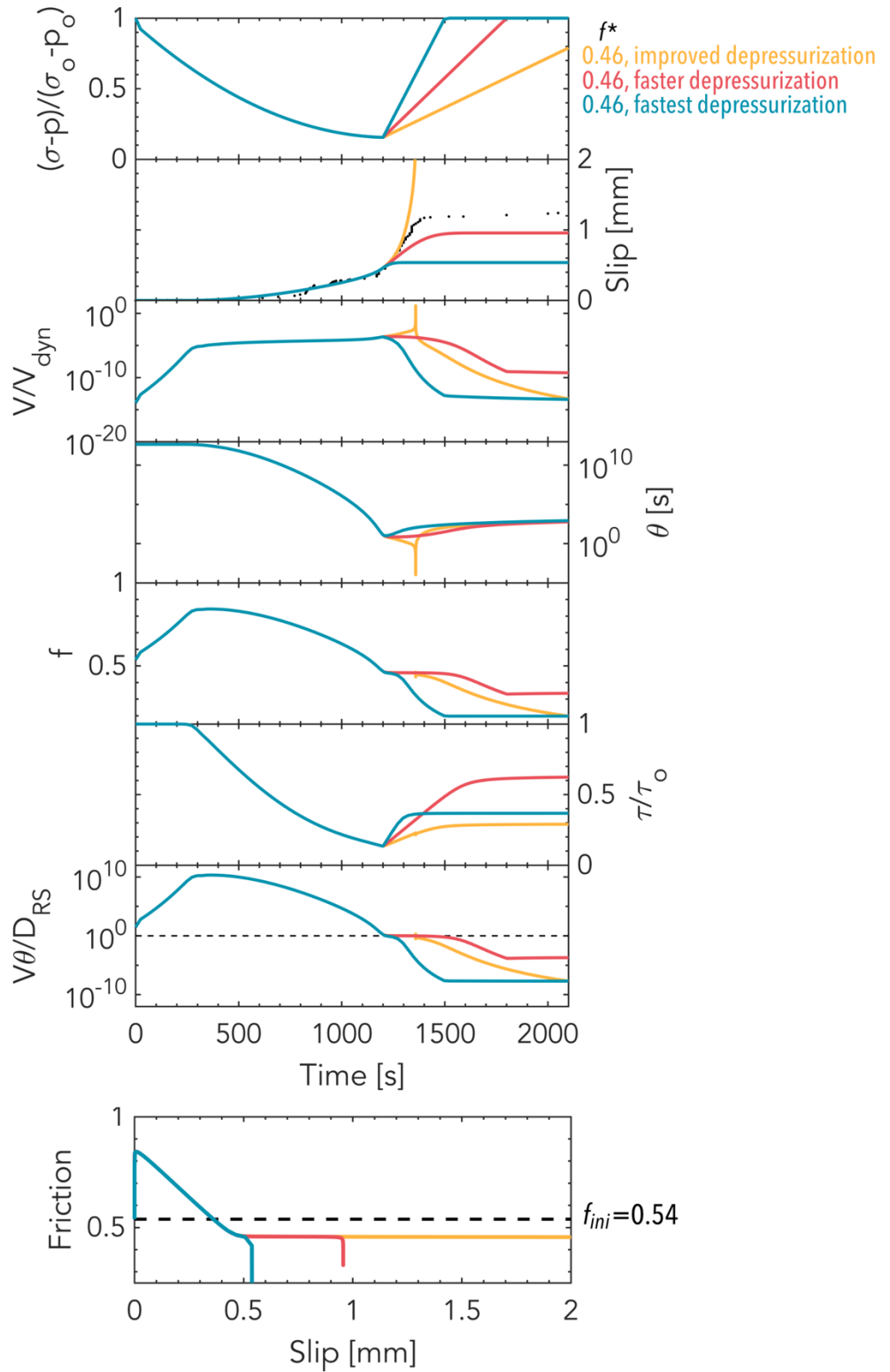
Figure S29. Effect of varying depressurization rate on a case similar to the low-friction case but with an even lower f^* of 0.46. In this case, the depressurization applied as in Figure 2 in the main text is not sufficient to prevent earthquake nucleation (yellow curve). The other two faster depressurization rates successfully suppress the earthquake (pink and turquoise curves).